JOURNAL OF GEOPHYSICAL RESEARCH, VOL. 105, NO. E4, PAGES 9701–9716, APRIL 25, 2000

Thermal infrared emission spectroscopy of the pyroxene mineral series

Victoria E. Hamilton

Department of Geology, Arizona State University, Tempe

Abstract. The thermal infrared emissivity spectra of coarse particulate samples of compositions in the pyroxene series display reststrahlen features (absorptions) that distinguish not only orthorhombic from monoclinic structures, but also major end-members within the two structural groups, as well as minerals within solid solution series. The exact number of reststrahlen features observed and their positions are dependent on mineral structure and cation occupancy of the M1 and M2 sites. End-member quadrilateral pyroxenes ($Mg_2Si_2O_6$-$Fe_2Si_2O_6$-Ca[Mg, Fe]Si_2O_6) are easily distinguished from each other and from minerals in the nonquadrilateral series ($NaFeSi_2O_6$-Na[Al, Fe]Si_2O_6-$LiAlSi_2O_6$). Furthermore, among quadrilateral pyroxenes, variations in Mg/(Mg + Fe) are linearly correlated with several band locations, as are variations in Ca content in high-Ca clinopyroxenes. In both quadrilateral and nonquadrilateral compositions, Christiansen feature positions are also diagnostic. No correlations with minor constituents (of the order of 0.05 atoms per formula unit) were observed. The detailed spectral characteristics of pyroxenes and their variability as a function of structure and cation occupancy are presented here with determinative curves for the identification of pyroxene composition. These data have important implications for the interpretation of spectral data from both laboratory and remote sensing instruments because they should permit a more detailed determination of pyroxene composition in measured unknown pure mineral and bulk compositions dominated by surface scattering, i.e., all particulates greater than ~65 μm, and solid samples.

1. Introduction

Pyroxenes are important rock-forming minerals that have a wide range of compositions and are found primarily in rocks derived from igneous and metamorphic processes. Due to their geological importance, pyroxenes have been the subject of numerous spectroscopic studies in the visible (V), near infrared (NIR), and thermal infrared (TIR) regions of the electromagnetic spectrum. Electronic spectroscopy (VNIR) examines electron transitions and crystal field effects in minerals, and numerous electronic spectroscopy studies have produced a large quantity of literature describing the major and trace element systematics of pyroxene minerals [e.g., *Adams*, 1974; *Bancroft and Burns*, 1967; *Evans et al*., 1967; *Goldman and Rossman*, 1979; *Rossman*, 1974; *Virgo and Hafner*, 1970]. *Cloutis and Gaffey* [1991] provide an excellent review of these studies and the relationships between spectral features and compositional variations observable in the ~0.3 to ~2.6 μm region of the electromagnetic spectrum.

Fundamental vibrations of atoms in the crystal lattices of most minerals absorb incident electromagnetic energy at frequencies which coincide with the middle, or TIR portion of the electromagnetic spectrum (greater than ~5 μm); in some minerals, diagnostic absorptions due to vibrational overtones and combinations can be present at shorter wavelengths, but the absorption coefficients of such bands are weaker than those resulting from the fundamental vibrations. In the laboratory work described here, absorption features with wavenumbers between ~2000 and 400 cm^{-1} (corresponding to wavelengths of 5–25 μm) are studied. Within this wavelength range, virtually all minerals have a unique set of spectral absorption features that allow them to be distinguished from each other. Thus the TIR region of the spectrum is excellent for examining pure samples as well as mineralogically complex geologic materials (i.e., rocks) and is gaining popularity as a remote sensing wavelength range for geologic applications [e.g., *Palluconi and Meeks*, 1985; *Christensen et al*., 1992].

Previous TIR spectral studies of pyroxene minerals commonly focused on either calculations of the vibrational frequencies of pyroxenes [*Saksena*, 1961; *Gaskell*, 1967; *Lazarev*, 1972], comparisons between chain silicates with differing numbers of anions in the repeat units [*Lazarev and Tenisheva*, 1961a, b; *Ryall and Threadgold*, 1966], investigations of a single pyroxene [*Omori*, 1971], comparisons of pyroxene minerals to other silicates [*Launer*, 1952], or on the spectral variability between members of one of the several pyroxene solid solution series (e.g., clinopyroxenes) [*Rutstein and White*, 1971; *Estep*, 1972; *Estep et al*., 1971, 1972]. Most previous studies have used transmission or Raman techniques, both of which produce different spectral features than the emission technique; emission or reflectance measurements were not necessary, as the results of these investigations were not intended to be applied to remote sensing data. To our knowledge, there are no studies of pyroxenes in the TIR, using either an emission or hemispherical reflectance technique, that attempt to describe the systematics of varied pyroxene spectra as a function of composition and structure. Emission (or hemispherical reflectance) data of minerals and rocks are valuable to geologists for several reasons, including (1) the time required for analysis of

Paper number 1999JE001112.
0148-0227/00/1999JE001112$09.00

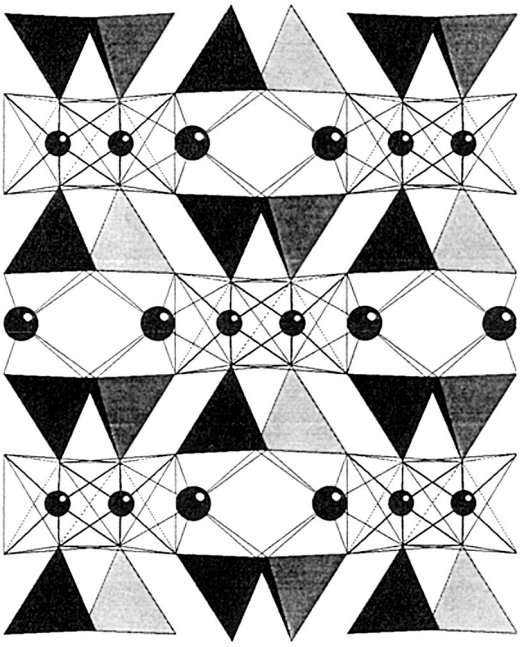

Figure 1. Diagram of the pyroxene I-beam structure. View is down *c* axis. Small atoms represent M1 site, and large atoms represent M2 site.

unknown mineral and rock (e.g., field) samples can be significantly reduced because sample preparation is not required, and (2) laboratory emission (hemispherical reflectance) data provide convenient libraries for direct comparison to data acquired by field spectrometers and airborne or orbital remote sensing instruments.

The objective of this work is to provide a comprehensive analysis of the TIR spectral characteristics of major end-members and common compositions in the pyroxene mineral series as a function of structure and composition. We first review pyroxene crystal chemistry and the theory of vibrational spectroscopy as well as its prior application to pyroxene mineralogical analysis. We then list the pyroxene samples used in this study and their compositions as determined by electron microprobe analyses. In the Results section, we discuss our spectral analysis of quadrilateral and non-quadrilateral (Na- and Li-bearing) pyroxene compositions as a function of crystal structure and chemistry. Finally, we summarize the applicability of these results to the identification of unknown samples and examine the effect of reduced spectral resolution, which has implications for the accuracy of identifications in many remote sensing datasets.

2. Background

2.1. Pyroxenes

Pyroxenes are silicate minerals with a general formula of XYZ_2O_6, where X represents Na^+, Ca^{2+}, Mn^{2+}, Fe^{2+}, Mg^{2+}, and Li^+ in the M2 site; Y represents Mn^{2+}, Fe^{2+}, Mg^{2+}, Fe^{3+}, Al^{3+}, Cr^{3+}, and Ti^{4+} in the M1 site; and Z represents Si^{4+} and sometimes Al^{3+} [*Cameron and Papike*, 1981]. The most common pyroxenes are part of the chemical group known as quadrilateral pyroxenes [*Papike et al*., 1974] with the monoclinic (clinopyroxene) end-members diopside, $CaMgSi_2O_6$, and hedenbergite, $CaFe^{2+}Si_2O_6$, and the orthorhombic (orthopyroxene) end-members enstatite, $Mg_2Si_2O_6$, and ferrosilite, $Fe_2^{2+}Si_2O_6$. Compositions containing 5–15 mol % Ca are referred to as pigeonite. Pigeonites are monoclinic but belong to a different space group than the high-Ca clinopyroxenes. Non-quadrilateral pyroxene compositions contain formula cations other than those of the end-member quadrilateral compositions, such as Fe^{3+}, Mn^{2+}, Na^+, and Li^+. Mineral compositions in this category include johannsenite, $Ca(Mn, Fe)Si_2O_6$, omphacite, $(Ca, Na)(Mg, Fe^{2+}, Fe^{3+}, Al)Si_2O_6$, acmite, $NaFe^{3+}Si_2O_6$, jadeite, $NaAlSi_2O_6$, and spodumene, $LiAlSi_2O_6$. In this study, we will examine minerals in both chemical groups with an emphasis on quadrilateral compositions.

The ideal pyroxene structure is based on two tetrahedral chains and one octahedral strip that form an "I-beam" unit [*Klein and Hurlbut*, 1993]. The tetrahedral chains consist of silicon-oxygen (Si-O, or generically "T-O") tetrahedra linked at two corners to form an infinite chain $(SiO_3)^{2-}$ along the c axis of the crystal with two tetrahedra in the repeat unit. The tetrahedra are arranged such that their bases are approximately parallel to the (100) plane. Octahedral layers contain 6- or 8-coordinated metal cations; the M1 site is in 6-fold coordination with the oxygens, and the coordination of the M2 site (6-, 7-, or 8-fold) is determined by the size of the cation. In the I-beam the two tetrahedral layers point toward each other and are cross linked by cations in the octahedral layers. The M1 cations lie between the apices of the SiO_3 chains, and the M2 atoms lie between the bases of the I-beams (Figure 1). The stacking arrangement of the tetrahedral and octahedral layers determines the symmetries of the various structures. The remainder of this section is a summary of the crystal chemistry of pyroxenes as discussed in detail by *Cameron and Papike* [1981].

Pyroxene structures are either monoclinic (clinopyroxene) or orthorhombic (orthopyroxene). Natural compositions containing only Mg and/or Fe^{2+} in the M1 and M2 sites belong to the predominant orthorhombic space group, *Pbca*. The high-Ca monoclinic pyroxenes belong to space group *C*2/*c*, and pigeonites belong to space group $P2_1/c$. Although the ideal pyroxene tetrahedral chain has 180° bond angles between adjacent tetrahedra, real minerals rarely exhibit such perfection, instead having distorted and/or rotated tetrahedra. Rotations may tend toward cubic close-packing and/or hexagonal close-packing within a space group. Within the *Pbca* structural type, the two chains of an I-beam are kinked by slightly different amounts and are not symmetrically equivalent (one chain, A, is more extended and has smaller tetrahedra than the other, B, which is more kinked). These distortions and rotations of the tetrahedra are due to several effects, including shared polyhedral edges, the size and charge of the octahedral cations, and the coordination and local electrostatic environment of the oxygen atoms. However, both chains exhibit rotations that lead to cubic close-packing. The *C*2/*c* pyroxenes have chains that are symmetrically equivalent and also tend toward cubic close-packing rotations. Pigeonite (space group $P2_1/c$) has asymmetric chains, one of which exhibits cubic close-packing rotations, and another that exhibits hexagonal close-packing rotations. The octahedral layers of each space group are also "skewed" or "tilted." *Pbca* pyroxenes exhibit alternating directions of skew, while octahedral strips in *C*2/*c* and $P2_1/c$ pyroxenes exhibit only one direction of skew. Lastly, the structural configuration of the M2 site is variable, resulting in either shared tetrahedral/octahedral edges or no shared edges. When there are no shared edges, the M2 site is largest and is most stable. If there are shared edges, the M2 polyhedron is smallest. *Pbca* and

$P2_1/c$ pyroxenes have some shared edges and therefore smaller M2 sites than $C2/c$ pyroxenes, which have no shared edges.

2.2. Theory of Vibrational Spectroscopy

Crystalline solids are composed of a regular, repeating pattern of positive and negative ions that vibrate at quantized frequencies. When the positive and negative ions move out of phase with each other, absorption of energy becomes possible at the wavelength corresponding to the vibrational frequency of the motions, as long as there is a net dipole moment. For example, in silicate minerals the primary spectral absorptions (reststrahlen bands) are due to the stretching and bending motions in the silicon-oxygen anions. Additional absorption features result from metal-oxygen and lattice vibrations. The exact frequencies, shapes, intensities, and number of features in a mineral's spectrum are dependent on the relative masses, radii, distances, and angles between atoms and their bond strengths. These parameters are determined by the structural arrangement of the anions (i.e., their polymerization), and the location and composition of the cations associated with them. Because all minerals consist of unique structures and/or compositions, virtually every mineral has a different suite of vibrational absorption characteristics and thus a unique spectrum in the thermal infrared.

3. Pyroxene Sample Preparation and Chemistry

Pyroxene samples used in this study have been crushed, sieved, and handpicked to include only (visibly) pure grains ranging in size from 710 to 1000 μm (1 mm). This particle size range was chosen to match the particle size used in the Arizona State University (ASU) spectral library [*Christensen et al*., this issue (b)] and to avoid spectral effects due to volume scattering that may occur in spectra of very fine particulate samples (greater than ~65 μm). The results in this study are applicable to samples dominated by surface scattering, with particle sizes greater than at least 65 μm, including solid samples (the spectra of particulate samples vary from solid samples only in spectral contrast, with no variation in band location or shape). All samples except two are natural samples; the author generated the synthetic diopside sample (VEH-DIO01) at ASU, and the pigeonite sample ($Wo_{15}En_{36}Fs_{54}$ 33,34) was synthesized by D. Lindsley at the State University of New York, Stony Brook. Numerous samples were graciously loaned by the National Museum of Natural History at the Smithsonian Institution (sample numbers beginning NMNH), while others were loaned by the Los Angeles County Natural History Museum (LACMNH), the U.S. Geological Society (USGS) Spectroscopy Lab, Denver (HS, Hunt and Salisbury Collection), or purchased from Ward's Natural Science (WAR), David Shannon Minerals (DSM), and Burminco (BUR). Many of these samples are included in the ASU Thermal Emission Spectroscopy Laboratory's mineral library [*Christensen et al*., this issue, (b)]. Sample purity was verified through one or more of the following techniques: electron microprobe, X-ray diffraction, and bulk chemical analysis. All samples and their chemistries are listed in Table 1, with a quality rating from 1 to 4. A quality rating of 1 indicates a pure sample, without any exsolved phases or significant substitutions. A rating of 2 indicates minor compositional impurities (including observed exsolution) having no significant observable effect on the mineral spectrum, and a designation of 3 is given when the sample is too impure to include in the data analysis. A rating of 4 is given to samples that do not have compositional data but appear physically and spectrally to be high-quality samples. The compositions of quadrilateral pyroxenes are plotted on the pyroxene ternary in Figure 2, and representative spectra of both quadrilateral and nonquadrilateral compositions are shown in Figure 3. Table 2 contains the weight percent (wt %) oxide data for each sample. Although iron content is usually reported as wt % FeO, electron microprobe analyses cannot distinguish between Fe^{2+} and Fe^{3+}. In converting each mineral's analysis from wt % oxides to mole percent (mol %) a test was performed to determine whether or not any or all of the measured FeO should be reallocated to Fe_2O_3 prior to the conversion [*Droop*, 1987]. For samples in which the occurrence of Fe^{3+} is unlikely, any indication of reassignment is assumed to be in error, whereas for samples with increased abundances of elements that make paired substitutions, the reassignment is judged to have a greater likelihood of reflecting the true valence states of Fe in the mineral. This study does not attempt to discriminate between variabilities in spectral character due to Fe valency, merely those related to overall abundance; in the future, we will examine the pyroxene spectra for these effects after obtaining visible/near infrared and Mössbauer spectroscopic analyses for Fe valency determination.

At the time of this writing, no enstatite samples with $>Mg_{94}$ or $<Mg_{65}$ were available; as the ASU collection expands and additional high- and low-Fe samples are obtained, their characteristics will be added to the data here, and the trends reevaluated. Some compositions, such as those with $<Mg_{50}$, are uncommon, and others ($<Mg_{10}$) are rare in nature and likely will be difficult to obtain. Unfortunately, due to the extreme difficulty encountered in obtaining a pure, uninverted sample of pigeonite, only a single, synthetic sample is included in this study, and thus the variability of this mineral's spectral characteristics cannot be addressed by this study. Because the discussion of pigeonite is limited, references to "clinopyroxene" should be taken as equivalent to "high-calcium" pyroxene, unless otherwise stated.

4. Thermal Infrared Spectral Data Acquisition

The spectrometer used in this study is a Mattson Cygnus 100 Fourier transform infrared (FTIR) interferometric spectrometer that has been modified to measure emitted sample radiance. A detailed description of the emission technique and the ASU spectrometer is provided by *Ruff et al*. [1997]. The sample chamber is located within a glove box that is external to the spectrometer; both the glove box and the spectrometer are constantly purged to remove as much atmospheric H_2O and CO_2 as possible. Particulate samples are poured into copper sample cups, which are painted IR black and have a 3-cm internal diameter. The spot size observed is ~1 cm, with the goal of obtaining a spectrum that is representative of many randomly oriented grains. Consistency of spectral features between samples and over multiple analyses indicates that this goal is achieved. Prior to analysis, particulate pyroxene samples were heated to 80°C to improve signal to noise during data acquisition. This temperature was maintained throughout data acquisition by the use of a controlled heater element underneath the sample cup. Spectral data were collected over the wavelength range of 2000–400 cm^{-1} (5–25 μm) at a spectral sampling of 2 cm^{-1}; however, data in the 2000–1400 cm^{-1} region typically are not shown because there are few well-resolved silicate absorption features and residual water vapor

Table 1. Pyroxene Sample Information

Sample	Mineral	Chemical Formula*	Quality	Locality	Notes
BUR-1820	clinopyroxene	$(Ca_{.99}Mg_{.91}Fe^{2+}_{.08}Na_{.02})Si_2O_6$	1	Otter Lake, Ontario, Canada	
BUR-1920	orthopyroxene	$(Ca_{.03}Mg_{1.51}Fe^{2+}_{.42})Al_{.02}Si_{1.98}O_6$	1	Stillwater Complex, Montana	
BUR-2883	johannsenite	$(Ca_{1.01}Mn_{.72}Mg_{.12}Fe^{2+}_{.13}Fe^{3+}_{.05})Si_{1.98}O_6$	1	Graham Co., Arizona	
BUR-620	clinopyroxene	$(Ca_{.88}Mg_{.43}Fe^{2+}_{.32}Fe^{3+}_{.20}Na_{.14}Mn_{.02})Al_{.07}Si_{1.93}O_6$	1	Verona, Ontario, Canada	
DSM-AUG01	clinopyroxene	$(Ca_{.85}Mg_{.83}Fe^{2+}_{.15}Fe^{3+}_{.11}Na_{.03}Ti_{.02})Al_{.13}Si_{1.87}O_6$	1	n/a	
DSM-DIO01	clinopyroxene	$(Ca_{.99}Mg_{.96}Fe^{2+}_{.02}Al_{.02})Si_2O_6$	1	n/a	
DSM-ENS01	orthopyroxene	$(Ca_{.01}Mg_{1.76}Fe^{2+}_{.19})Si_2O_6$	1	Preg Quarry, Kraubath, Styria, Austria	
DSM-HED01	clinopyroxene	$(Ca_{.98}Mg_{.26}Fe^{2+}_{.47}Mn_{.27})Si_2O_6$	1	Iron Cap Prospect, Graham Co., Arizona	Mn-rich
HS-10.4B	clinopyroxene	$(Ca_{.74}Mg_{.25}Fe^{2+}_{.61}Fe^{3+}_{.09}Mn_{.14}Na_{.11}Al_{.04})Si_2O_6$	2	Silver Star, Montana	
HS-119.4B	clinopyroxene	$(Ca_{.96}Mg_{.66}Fe^{2+}_{.24}Fe^{3+}_{.07}Na_{.05})Al_{.03}Si_{1.97}O_6$	1	Oaxaca, Mexico	
HS-15.4B	clinopyroxene	$(Ca_{.99}Mg_{.88}Fe^{2+}_{.05}Fe^{3+}_{.03}Na_{.03}Al_{.02})Si_2O_6$	1	Edwards, New York	
HS-199.4b	pigeonite	n/a	3	n/a	removed
HS-205.4b	clinopyroxene	$(Ca_{.83}Mg_{.71}Fe^{2+}_{.20}Fe^{3+}_{.10}Na_{.09}Al_{.05})Al_{.10}Si_{1.90}O_6$	3	Essex County, New York	removed
HS-210.4b	spodumene	$(Li_{.70}Al_{1.1})Si_2O_6$	1	Afghanistan	
HS-317.4B	clinopyroxene	$(Ca_{1.01}Mg_{.89}Fe^{2+}_{.07}Al_{.02})Si_2O_6$	2	Finland	
HS-9.4B	orthopyroxene	$(Ca_{.02}Mg_{1.77}Fe^{2+}_{.18}Fe^{3+}_{.02})Si_2O_6$	1	Jackson County, North Carolina	
LACMNH-6800	acmite	$(Na_{1.06}Fe^{3+}_{.92}Ca_{.23}Mg_{.04}Al_{.03})Si_2O_6$	1	Arkansas	
LACMNH-SPD01	spodumene	n/a	4	Pala, California	
NMNH-107497	clinopyroxene	$(Ca_{.99}Mg_{.98}Fe^{2+}_{.03})Si_2O_6$	1	Sinkhole Crater, Bandana, North Carolina	
NMNH-119197	clinopyroxene	$(Ca_{.94}Mg_{.80}Fe^{2+}_{.16}Fe^{3+}_{.03}Na_{.03}Al_{.03})Si_2O_6$	1	Eureka, Ducktown, Tennessee	
NMNH-119793	orthopyroxene	$(Ca_{.04}Mg_{1.68}Fe^{2+}_{.24}Al_{.04})Al_{.05}Si_{1.95}O_6$	1	Mount Davies, S. Australia	
NMNH-120414-1	orthopyroxene	$(Ca_{.03}Mg_{1.49}Fe^{2+}_{.46})Al_{.04}Si_{1.96}O_6$	2	Roding River, Nelson, New Zealand	cpx phase
NMNH-122302	clinopyroxene	$(Ca_{.86}Mg_{.75}Fe^{2+}_{.12}Fe^{3+}_{.15}Na_{.05}Al_{.05}Ti_{.03})Al_{.20}Si_{1.80}O_6$	1	Nasinu Village, Ovalau, Fiji	
NMNH-128288	orthopyroxene	$(Ca_{.04}Mg_{1.65}Fe^{2+}_{.26}Fe^{3+}_{.02})Al_{.03}Si_{1.97}O_6$	2	Frank Smith Mine, Barkly West, S. Africa	cpx phase
NMNH-16168	clinopyroxene	$(Ca_{.98}Mg_{.43}Fe^{2+}_{.48}Fe^{3+}_{.05}Mn_{.06})Al_{.02}Si_{1.98}O_6$	1	n/a	
NMNH-166555	orthopyroxene	$(Ca_{.01}Mg_{1.51}Fe^{2+}_{.39}Fe^{3+}_{.04}Al_{.05})Al_{.10}Si_{1.90}O_6$	2	Lac Onatchiway, Quebec, Canada	cpx phase
NMNH-34669	orthopyroxene	$(Mg_{1.82}Fe^{2+}_{.13}Fe^{3+}_{.05})Al_{.02}Si_{1.97}O_6$	1	Kupperburg, Bayem, Germany	
NMNH-38833	orthopyroxene	$(Ca_{.01}Mg_{1.76}Fe^{2+}_{.19}Fe^{3+}_{.03})Al_{.04}Si_{1.96}O_6$	1	Webster, North Carolina	
NMNH-80819	clinopyroxene	$(Ca_{.98}Mg_{.90}Fe^{2+}_{.06}Fe^{3+}_{.04})Al_{.04}Si_{1.96}O_6$	1	Schwartzenstein, Tyrol, Austria	
NMNH-82436	orthopyroxene	$(Ca_{.01}Mg_{1.76}Fe^{2+}_{.17}Fe^{3+}_{.05})Al_{.05}Si_{1.95}O_6$	1	Webster, North Carolina	
NMNH-93527	orthopyroxene	$(Ca_{.06}Mg_{1.43}Fe^{2+}_{.36}Fe^{3+}_{.05}Al_{.08})Al_{.14}Si_{1.86}O_6$	1	Paul's Island, Labrador, Canada	
NMNH-9780	clinopyroxene	$(Ca_{.85}Mg_{.54}Fe^{2+}_{.53}Na_{.03}Al_{.04})Al_{.03}Si_{1.97}O_6$	1	Berks Co., Pennsylvania	
NMNH-B18427	orthopyroxene	$(Ca_{.09}Mg_{1.22}Fe^{2+}_{.56}Fe^{3+}_{.03}Al_{.05})Al_{.11}Si_{1.89}O_6$	2	Heinola, Finland	
NMNH-C2368	orthopyroxene	$(Ca_{.08}Mg_{1.38}Fe^{2+}_{.44}Fe^{3+}_{.02}Al_{.07})Al_{.11}Si_{1.89}O_6$	1	western Greenland	
NMNH-R11524	clinopyroxene	$(Ca_{1.01}Mg_{.06}Fe^{2+}_{.78}Fe^{3+}_{.04}Mn_{.11})Al_{.01}Si_{1.98}O_6$	2	Baird, Shasta Co. California	Mn-rich
NMNH-R14440	orthopyroxene	$(Ca_{.01}Mg_{1.81}Fe^{2+}_{.15}Fe^{3+}_{.03})Si_2O_6$	1	Kraubat, Styria, Austria	
NMNH-R15161	clinopyroxene	$(Ca_{.97}Mg_{.87}Fe^{2+}_{.09}Fe^{3+}_{.04}Na_{.03})Al_{.02}Si_{1.98}O_6$	1	Templeton, Quebec, Canada	
NMNH-R17421	clinopyroxene	$(Ca_{.99}Mg_{.76}Fe^{2+}_{.21}Fe^{3+}_{.01})Si_2O_6$	1	Magog, Quebec, Canada	
VEH-DIO01	clinopyroxene	$(Ca_{.96}Mg_{.96}Fe^{2+}_{.02}Al_{.02})Al_{.02}Si_{1.98}O_6$	1	···	synthetic
WAR-2889	orthopyroxene	$(Ca_{.01}Mg_{1.75}Fe^{2+}_{.22})Si_2O_6$	2	Bramble, Norway	
WAR-5780	clinopyroxene	$(Ca_{.94}Mg_{.95}Fe^{2+}_{.01}Fe^{3+}_{.07}Na_{.03})Al_{.02}Si_{1.97}O_6$	1	Jaipur, India	
WAR-5858	clinopyroxene	$(Ca_{.79}Mg_{.93}Fe^{2+}_{.13}Fe^{3+}_{.10}Na_{.03}Ti_{.02})Al_{.13}Si_{1.87}O_6$	1	Tillamook Co., Oregon	
WAR-6454	clinopyroxene	$(Ca_{.96}Mg_{.98}Fe^{2+}_{.04}Na_{.03})Al_{.05}Si_{1.95}O_6$	1	Bird Creek, Ontario, Canada	
WAR-6474	clinopyroxene	$(Ca_{.86}Mg_{.56}Fe^{2+}_{.20}Fe^{3+}_{.20}Na_{.15}Al_{.02})Al_{.08}Si_{1.92}O_6$	1	Harcourt, Ontario, Canada	
WAR-7684	spodumene	n/a	1	Newry, Maine	
WAR-9909	jadeite	$(Na_{.93}Al_{.80}Fe^{3+}_{.09}Ca_{.09}Mg_{.08})Si_{1.98}O_6$	1	Monterey, California	
WAR-ACM01	acmite	$(Na_{1.16}Fe^{3+}_{.85}Ca_{.15}Mg_{.07}Al_{.03})Si_2O_6$	3	n/a	two phases
$Wo_{10}En_{36}Fs_{54}$ 33,34	pigeonite	>90% pig. w/minor quartz & olivine	1	···	synthetic

*Fe^{2+} and Fe^{3+} values are based on recalculation of wt % oxides (see Table 2).

features may be present. For each sample, 260 scans (collected over ~7 min) were averaged to produce a single spectrum. Raw radiance data were converted to emission spectra following the method of *Christensen and Harrison* [1993], as adapted by *Ruff et al*. [1997]. Sources of error in the acquisition of this data are described by *Ruff et al*. [1997]; the total instrument-derived emissivity error for any given spectrum in this study is ~2–5%, and reproducibility with this technique is better than 1%.

5. Results and Discussion

5.1. Quadrilateral Pyroxenes

Vibrational spectra of this suite of quadrilateral pyroxenes exhibit significant variations in emissivity due to both structural and compositional differences (Figure 3). In terms of structurally related differences, orthopyroxene spectra (enstatite in Figure 3) may be broadly described as having reststrahlen features in the 1200–800 cm^{-1} region that have the overall appearance of a broad absorption with three separate minima (the central of these three minima has two or four additional superposed minima), and additional reststrahlen features in the 600–400 cm^{-1} region, which have an overall V-shaped appearance. Quadrilateral clinopyroxenes ($C2/c$) may be broadly described as having two separate absorptions between 1200 and 800 cm^{-1}, with the one at longer wavelengths typically having two emission minima (diopside in Figure 3). In the 600–400 cm^{-1} region the combined absorptions lack the V shape of the orthopyroxenes, instead having a more rectangular shape with two or three superposed minima. Clinopyroxene spectra exhibit fewer minor band minima than the spectra of orthopyroxenes; this is probably directly related to the homogeneity and uniformity of the tetrahedral layers of the $C2/c$ pyroxenes, as described in section 2.1. The two symmetric $C2/c$ chains should generate virtually the same vibrational frequencies and thus a smaller total number of frequencies than the distinct A and B chains of the *Pbca* pyroxenes, which should have a greater number of differing vibrations due to the dissimilarity between the A and B chains. It is noteworthy that several samples obtained for this study arrived labeled as pyroxenes (presumably on the basis of a hand sample identification), but upon spectral analysis became suspect due to significant deviation from these basic spectral shapes. In fact, these suspect samples were subsequently identified as amphiboles and were probably formed by alteration of pyroxenes.

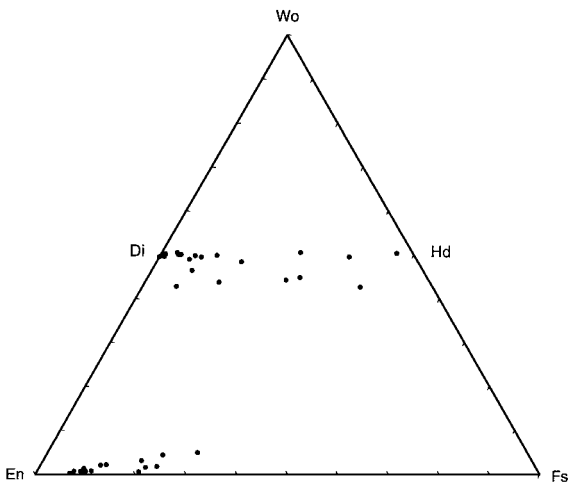

Figure 2. Ternary diagram showing compositions of pyroxenes used in this study.

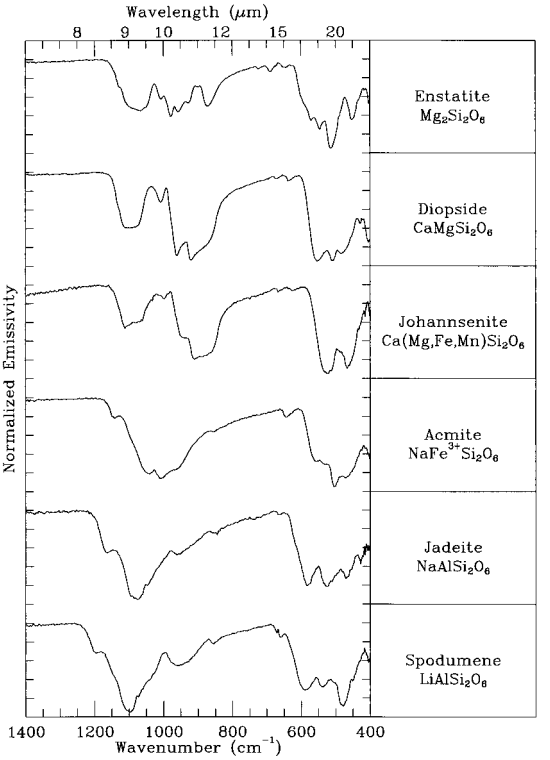

Figure 3. Emissivity spectra of major pyroxene compositions. Spectra in this and all other plots designated as such are normalized over the entire wavelength region.

Spectra of samples within the orthopyroxene and clinopyroxene solid solution series exhibit variations in the number of absorption features present and their wavelength positions, which provide further diagnostic information about the composition of the samples within these series. These features are not the actual vibrational frequencies of the mineral; overlapping bands produce band shape changes and shifts in apparent band minimum and may mask low-contrast features due to the complex, coupled interactions of vibrational oscillators. Therefore these bands cannot be deconvolved as is possible with VNIR spectra [e.g., *Sunshine et al*., 1990]. However, the emissivity minima are still directly related to the vibrational frequencies and are diagnostic, varying in position as a function of composition and structure. In order to discuss these spectral features in terms of their relative rather than absolute position, a scheme has been devised for describing the relative band locations of major features. Band minima that are consistently present in the spectra of a mineral type (e.g., orthopyroxenes) and have a $\Delta\varepsilon$ (where ε is emissivity) that is greater than 20% of the total spectral contrast are referred to as "critical absorptions" (CAs); the first critical absorption in a spectrum is always the shortest wavelength feature and is designated CA1, the longest wavelength feature of n features is designated CAn. There are no designations on the basis of relative importance or absolute band depth because these are subjective (importance) or variable (emissivity) parameters. Absorptions with $\Delta\varepsilon$ less than 20% of the total spectral contrast are excluded from the CA designation due to the fact that they may not be resolvable at lower spectral resolutions or are not

Table 2. Pyroxene Compositional Data From Microprobe Analysis

Sample	SiO_2	TiO_2	Al_2O_3	Cr_2O_3	Fe_2O_3*	FeO	MnO	MgO	CaO	Na_2O	K_2O	Total
BUR-1820	54.30	0.05	0.31	0.00	0.00	2.67	0.13	16.68	25.29	0.23	0.00	99.65
BUR-1920	54.45	0.15	0.97	0.00	0.00	13.76	0.28	27.88	0.77	0.01	0.00	98.27
BUR-2883	48.54	0.01	0.08	0.00	1.54	3.81	20.88	1.90	23.05	0.04	0.00	99.85
BUR-620	50.51	0.11	1.69	0.00	7.02	9.88	0.73	7.58	21.51	1.91	0.00	100.94
DSM-AUG01	50.27	0.83	2.93	0.03	3.98	4.74	0.26	15.01	21.26	0.41	0.00	99.72
DSM-DIO01	55.64	0.01	0.47	0.00	0.00	0.64	0.07	17.99	25.69	0.17	0.00	100.69
DSM-ENS01	58.51	0.01	0.25	0.00	0.00	6.49	0.17	34.19	0.24	0.00	0.00	99.85
DSM-HED01	49.96	0.01	0.06	0.00	0.00	14.14	7.99	4.32	22.80	0.11	0.00	99.39
HS-10.4B	48.53	0.02	0.80	0.04	2.95	17.77	4.12	4.07	16.88	1.43	0.15	96.77
HS-119.4B	52.87	0.02	0.92	0.00	2.61	7.85	0.29	11.91	24.08	0.65	0.00	101.22
HS-15.4B	54.60	0.01	0.47	0.00	1.12	1.52	0.19	16.23	25.35	0.45	0.00	99.93
HS-199.4b	51.79	0.25	0.50	0.00	0.34	26.08	0.50	19.43	1.12	0.02	0.00	100.03
HS-205.4b	51.74	0.40	3.55	0.00	3.87	6.47	0.13	12.88	21.04	1.23	0.00	101.31
HS-210.4b	64.94	0.04	28.31	0.00	0.00	0.44	0.20	0.00	0.00	0.10	0.00	94.03
HS-317.4B	54.43	0.00	0.42	0.00	0.00	2.22	0.06	16.22	25.77	0.15	0.00	99.27
HS-9.4B	57.87	0.02	0.99	0.00	0.62	6.32	0.17	34.86	0.67	0.00	0.00	101.52
LACMNH-6800	51.33	0.67	0.54	0.01	30.62	0.00	0.51	0.66	5.31	13.73	0.00	100.29
LACMNH-SPD01	...	...	...	...	...	...	...	...	...	...	...	...
NMNH-107497	54.99	0.01	0.31	0.00	0.36	0.51	0.02	18.17	25.40	0.10	0.00	99.86
NMNH-119197	53.32	0.02	0.78	0.00	0.88	5.15	0.58	14.42	23.49	0.46	0.00	99.10
NMNH-119793	55.66	0.11	2.27	0.00	0.00	8.08	0.17	32.29	1.03	0.02	0.00	99.62
NMNH-120414-1	53.94	0.04	1.28	0.00	0.00	15.28	0.30	27.42	0.88	0.00	0.00	99.14
NMNH-122302	47.97	1.03	5.77	0.00	5.20	3.83	0.27	13.36	21.33	0.66	0.00	99.41
NMNH-128288	56.00	0.06	1.54	0.00	1.16	7.01	0.10	26.78	6.57	0.81	0.00	100.03
NMNH-16168	50.40	0.01	0.29	0.01	1.80	14.61	1.69	7.36	23.30	0.19	0.00	99.66
NMNH-166555	49.33	0.04	15.89	0.00	0.00	8.98	0.20	17.54	7.33	0.18	0.00	99.50
NMNH-34669	57.03	0.00	0.39	0.00	1.91	4.64	0.15	35.46	0.11	0.01	0.00	99.70
NMNH-38833	56.39	0.02	1.08	0.00	1.20	6.59	0.15	33.83	0.30	0.00	0.00	99.05
NMNH-80819	53.66	0.05	0.88	0.00	1.44	1.94	0.15	16.57	24.97	0.13	0.00	99.80
NMNH-82436	55.93	0.01	1.12	0.00	1.49	5.38	0.13	31.40	4.16	0.04	0.00	99.66
NMNH-93527	51.84	0.35	5.28	0.00	1.84	12.13	0.23	26.76	1.46	0.07	0.00	99.97
NMNH-9780	51.00	0.20	1.55	0.00	0.00	16.52	0.46	9.42	20.49	0.33	0.02	99.99
NMNH-B18427	51.17	0.51	3.78	0.00	1.18	18.20	0.30	22.16	2.24	0.13	0.01	99.69
NMNH-C2368	51.88	0.32	4.24	0.00	0.63	14.52	0.25	25.34	2.05	0.03	0.01	99.26
NMNH-R11524	48.06	0.01	0.23	0.00	1.32	22.63	3.27	1.06	22.85	0.06	0.00	99.48
NMNH-R14440	57.25	0.02	0.33	0.00	1.24	5.09	0.12	35.21	0.32	0.01	0.00	99.59
NMNH-R15161	54.06	0.03	0.71	0.00	1.31	2.78	0.17	15.86	24.75	0.37	0.00	100.04
NMNH-R17421	53.31	0.01	0.32	0.00	0.26	6.79	0.46	13.70	24.70	0.06	0.00	99.61
VEH-DIO01	54.82	0.01	0.92	0.07	0.00	0.68	0.01	17.75	24.73	1.28	0.00	100.27
WAR-2889	57.69	0.06	0.14	0.00	0.00	7.46	0.03	33.80	0.36	0.02	0.00	99.56
WAR-5780	54.14	0.02	0.51	0.00	2.56	0.26	0.06	17.54	24.25	0.45	0.00	99.80
WAR-5858	50.58	0.79	3.23	0.00	3.42	4.05	0.16	16.82	19.81	0.36	0.01	99.21
WAR-6454	53.88	0.06	1.19	0.00	1.58	0.00	0.08	18.12	24.76	0.41	0.01	100.09
WAR-6474	50.60	0.18	2.35	0.00	6.99	6.29	0.30	9.96	21.13	2.00	0.00	99.80
WAR-7684	...	...	...	...	...	...	...	...	...	...	...	...
WAR-9909	58.84	0.36	20.72	0.00	3.56	0.29	0.04	1.66	2.42	14.26	0.00	102.15
WAR-ACM01	52.01	2.48	0.60	0.00	28.25	0.00	0.43	1.14	3.46	15.06	0.00	100.29
$Wo_{15}En_{36}Fs_{54}$33,34	...	...	...	...	...	...	...	...	...	...	...	...

Values are in units of wt % oxide.
*Fe_2O_3 is obtained by recalculation [*Droop*, 1987].

present in every specimen of a similar composition. Figures 4 and 5 show representative spectra for two orthopyroxenes and two clinopyroxenes along with their critical absorptions. In the following discussion of absorption band variability, features will be referred to primarily by their CA designation.

There are four bands in the spectra of quadrilateral pyroxenes having $\Delta\varepsilon$ that are greater than 20% of the spectral contrast but that are not considered critical absorptions. These special cases and their significance to mineral identification and discrimination are discussed in detail below.

5.2. Orthopyroxenes

Orthopyroxene spectra exhibit characteristic variations in band presence (or absence) and the positions of emission minima and maxima. Table 3 lists the locations of absorption band minima and statistics for the critical absorptions of the orthopyroxenes studied. At a spectral sampling of 2 cm^{-1}, the theoretical error in band minimum selection is ± 2 cm^{-1}, al-

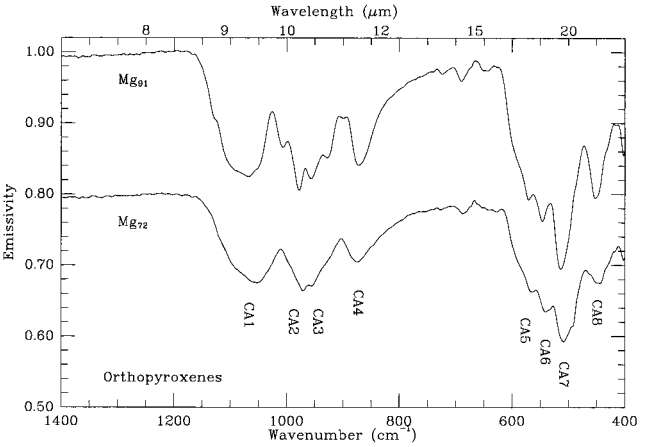

Figure 4. Locations of critical absorptions in orthopyroxenes. Mg_{72} spectrum is offset by 0.2 for clarity.

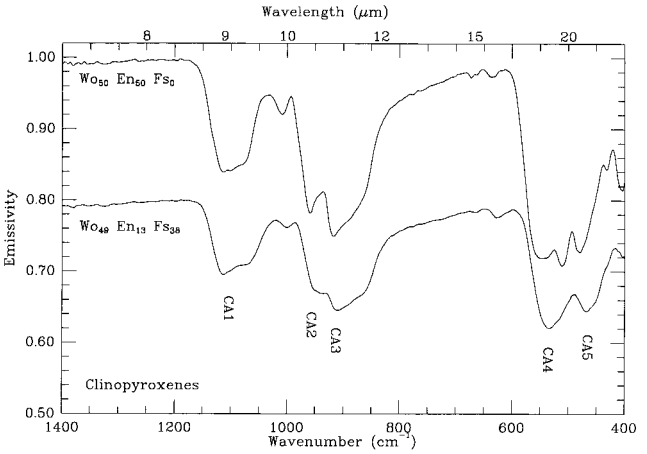

Figure 5. Locations of critical absorptions in clinopyroxenes. $Wo_{49}En_{13}Fs_{38}$ spectrum is offset by 0.2 for clarity.

though this error may be increased slightly in selecting the minima of broad bands. Variations in these band positions will be discussed from short to long wavelengths or in order of increasing CA number. Orthopyroxene compositions are described by the molecular percentage (mol %) of the Mg end-member; specimens in the sample collection represent compositions between Mg_{93} and Mg_{65}.

5.2.1. Critical absorption variation with Mg-Fe substitution. An overall decrease in spectral contrast is observed in the spectra of orthopyroxenes as samples become more Fe-rich (Figure 6), but there are additional diagnostic changes that allow compositional assignment on the basis of spectral characteristics. CA1 changes position as well as shape with increasing Fe content. The CA1 band minimum can be difficult to determine in the most Mg-rich samples due to its broadness (reflected in the standard deviation of the average band position). With increasing Fe, particularly in samples with Mg_{85} or lower, CA1 becomes narrower and increasingly asymmetric, with the band minimum being positioned on the long-

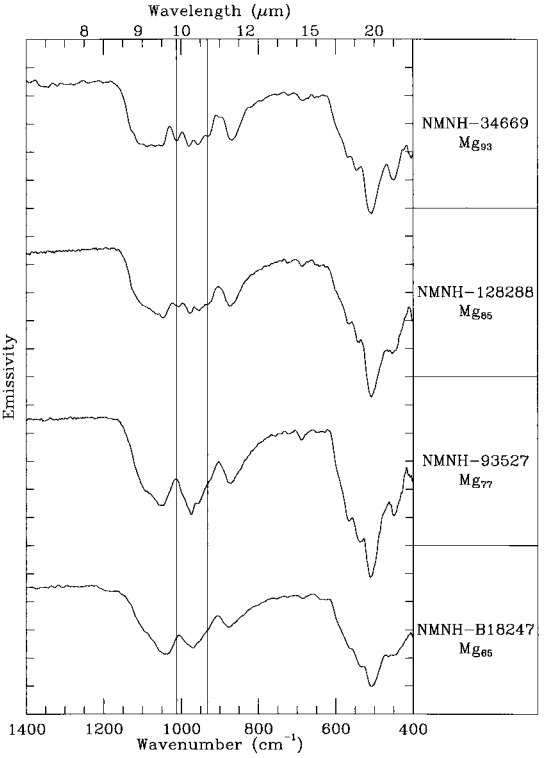

Figure 6. Emissivity spectra of orthopyroxenes along the Mg-Fe join. Spectra are plotted in decreasing order of Mg number. Vertical lines denote the positions of bands present only in Mg-rich samples. Each tick along the *y* axis represents a $\Delta\varepsilon$ of 0.04.

wavelength side of the feature (Figure 6). Additionally, the band minimum is located at increasingly longer wavelengths with increasing Fe, although above Mg_{85}, the band minimum is variable (Figure 7a).

The wavelength position of CA2 also increases with increasing Fe (Figure 7b). Above Mg_{90}, as with CA1, this trend does

Table 3. Positions of Critical Absorptions in Orthopyroxenes

		Band Position, cm^{-1}									
Sample	Mg/(Mg+Fe)	CA1	10 cm^{-1}	CA2	10 cm^{-1}	CA3	CA4	CA5	CA6	CA7	CA8
NMNH-34669	0.91	1090	1069	980	984	957	868	570	548	511	451
NMNH-R14440	0.91	1071	1069	979	984	959	872	571	547	514	452
DSM-ENS01	0.90	1099	1100	976	973	956	871	569	547	514	451
HS-9.4B	0.90	1072	1071	978	974	957	871	571	547	515	453
NMNH-82436	0.89	1067	1069	978	974	957	872	570	547	514	453
NMNH-38833	0.89	1064	1060	978	974	956	871	570	547	514	451
WAR-2889	0.89	1053	1054	979	984	958	874	570	547	514	451
NMNH-119793	0.88	1070	1070	978	953	956	872	570	547	514	452
NMNH-128288	0.85	1048	1048	977	974	955	873	566	542	509	453
NMNH-166555	0.78	1049	1049	974	974	957	873	567	534	512	452
BUR-1920	0.78	1053	1056	975	974	957	881	562	542	513	452
NMNH-93527	0.78	1051	1050	974	974	957	873	566	537	511	451
NMNH-120414-1	0.76	1040	1037	972	974	956	879	562	537	507	457
NMNH-C2368	0.75	1052	1056	971	974	955	874	563	542	508	447
NMNH-B18427	0.67	1040	1044	970	974	954	874	563	536	508	465
Average		1061	1060	976	975	956	873	567	543	512	453
Standard deviation		17	15	3	7	1	3	3	5	3	4
Minimum λ		1040	1037	970	953	954	868	562	534	507	447
Maximum λ		1099	1100	980	984	959	881	571	548	515	465
Δλ		59	63	10	31	5	13	9	14	8	18

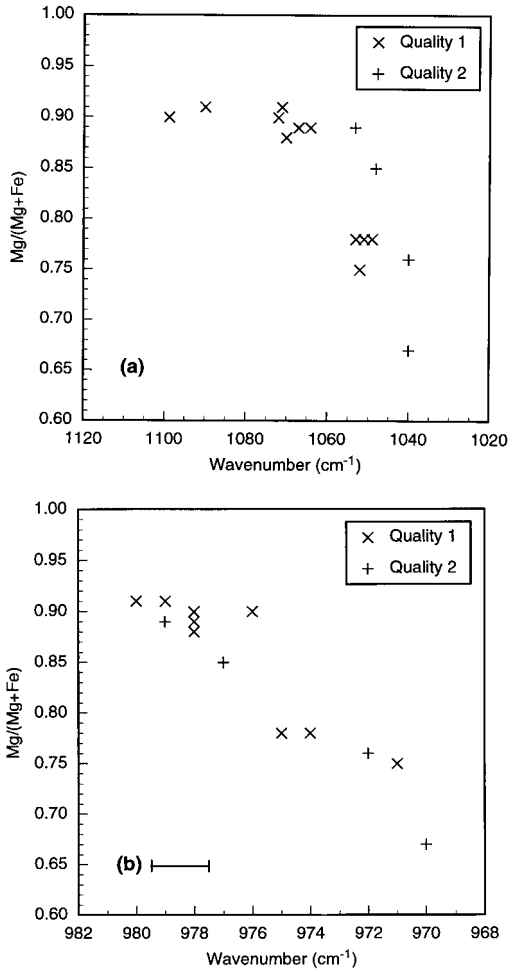

Figure 7. (a) Scatterplot of orthopyroxene CA1 band position versus Mg/(Mg + Fe). The *x* axis in this and subsequent scatterplots is shown in order of increasing wavelength (decreasing wavenumber) for consistency with spectral plots. Error bars along the wavenumber axis are smaller than the dimension of the symbols. (b) Orthopyroxene CA2 band position versus Mg/(Mg + Fe). Representative error bar is shown in the lower left corner of the plot.

not continue; instead, the position of the band becomes variable independent of composition. Until samples closer to 100% Mg can be examined, Mg_{90} must be considered the threshold for which this correlation holds true.

CA3 does not exhibit as clearly the same trend that CA1 and CA2 do. The location of this band is consistently near 956 cm^{-1}, such that in 14 samples, the range of values only varies by 5 cm^{-1}, which is near the spectral resolution (4 cm^{-1}) of the data (Table 3). If a similar trend is present in CA3, it may only be more clearly observed at a greater spectral resolution.

Another trend related to relative Mg-Fe content that is observed is broadening and shallowing of the CA4 feature at ~870 cm^{-1} (Figure 6). Much like the trend observed for the band position of CA1, CA4 band depth ($\Delta\varepsilon$, measured from the emissivity maximum between CA3 and CA4 to the CA4 band minimum) increases with increasing Mg content in a generally linear fashion up to Mg/(Mg + Fe) of about 0.90, at which point, the trend flattens (Figure 8a). The width of CA4 decreases with increasing Mg content, also in a generally linear fashion (Figure 8b). Similar trends in the broadening and weakening of this band were observed in natural and synthetic samples studied by *Estep et al*. [1971]. Similarly, weak minor bands in the 800–600 cm^{-1} region resulting from symmetric T-O-T stretching vibrations also exhibit a weakening in band strength with increasing Fe.

Critical absorptions in the long-wavelength reststrahlen bands (CA5–CA8) exhibit very little deviation in their wavenumber position as a function of Mg/(Mg + Fe), but two features do display changes in spectral contrast. CA6 and, in some but not all samples, CA8 (~545 and ~450 cm^{-1}) are reduced in spectral contrast as ferrosilite content increases, and CA8 may be broadened as well (Figure 6). Decreasing strength of CA8 with increasing ferrosilite content was observed by *Estep et al*. [1972] in connection with increasing disorder in the Fe^{2+} distribution over the M1 and M2 sites due to rapid quenching from high temperature. This disorder affects cation-oxygen stretching vibrations, bending vibrations of Si-O-Si groups in the silicate chain, and lattice modes, all of which result in absorptions in the 600–400 cm^{-1} region. This disorder and related spectral trend also can be correlated with increasing degrees of shock in meteoritic or lunar samples [*Estep et al*., 1972]. However, based on the relatively large

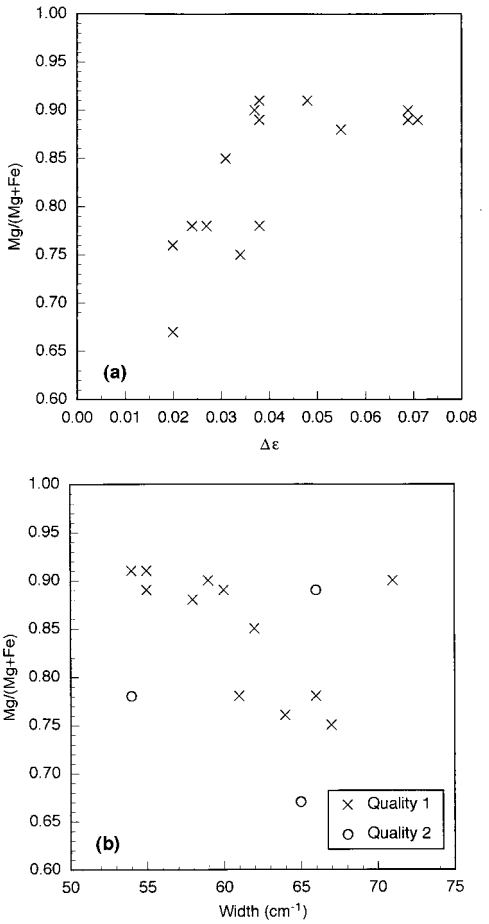

Figure 8. (a) Scatterplot of orthopyroxene CA4 band depth versus Mg/(Mg + Fe). (b) Scatterplot of orthopyroxene CA4 band width versus Mg/(Mg + Fe). Width is determined by the difference (in cm^{-1}) between the emissivity maximum on the short-wavelength side of CA4 and the spectral point having the same emissivity on the long-wavelength side of CA4. Several outlier points are identified as Quality 2 samples and may not accurately represent the actual trend of the data.

crystal size of the samples in this study, quenching seems unlikely, and shock can also be eliminated. Therefore caution should be used in applying the spectral contrast of CA8 as a measure of Fe content, temperature-related disorder, or significant shock pressures.

5.2.2. Additional (noncritical) features. Two small, sharp absorptions in Mg-rich orthopyroxene spectra, near 1010 and 929 cm^{-1} (denoted by vertical lines in Figure 6), are not consistently present in all orthopyroxene spectra. With increasing Fe content, these bands are reduced in emissivity, and in samples with compositions between Mg_{84} and Mg_{80} and lower, the bands are reduced to weak shoulders or disappear completely.

5.2.3. Additional cation substitution. All of the variability described above is correlated with relative Mg/Fe content. Orthopyroxenes can have up to ~5 mol % Ca, but no correlations between Ca content and band positions or shapes were observed, suggesting that small changes in Ca abundance (±2–3 mol %) are not enough to produce significant variations in the structure and thus the spectral character of orthopyroxenes. Substitution of Al for Si in the tetrahedral site is also common in orthopyroxenes, but no trends related to Al content were observed. Significant changes in T-O distance as a function of Al/(Al + Si) are known to occur (0 to ~0.375 Al/(Al + Si)), but are not as well defined for orthopyroxenes as for clinopyroxenes [*Cameron and Papike*, 1981]; however, based on the somewhat limited range of Al/(Al + Si) for this set of orthopyroxenes (0.01–0.07), it is likely that such a trend would not be visible in this data set (see also discussion of Al substitution in clinopyroxenes, below).

5.2.4. Discussion. There are several characteristics of orthopyroxene spectra that are variable with increasing Fe content in the mineral, but no significant variations with increasing Ca or Al abundances were observed. Three parameters, namely, CA1 position, the presence or absence of bands at 1010 and 929 cm^{-1}, and the wavenumber position of CA2, may be plotted as functions of Mg/(Mg + Fe), and these plots may be used to approximately determine the composition of an unknown orthopyroxene. Scatter in the data is probably largely due to the cumulative effect of minor impurities in each sample or, in other words, natural variability. Although the observed absorption band variations have been presented as correlating with Mg/(Mg + Fe), it is important to recall that these band variations are an indirect result of cation substitution on the T-O stretching vibrations. The majority of Mg-Fe substitutions occur in the octahedral layer, and because Fe^{2+} has a larger ionic radius than Mg^{2+}, the effect of substituting greater amounts of Fe^{2+} for Mg^{2+} in M2 is to progressively increase the size of the M2 octahedron. As the octahedron enlarges, it forces the A and B tetrahedral chains to straighten up to 10° and 5°, respectively [*Cameron and Papike*, 1981]. As the chain straightens, the mean T-O and mean bridging T-O bond lengths decrease. As the T-O bonds shorten (and presumably strengthen), their frequencies of vibration are expected to increase. However, the observed trends are in direct opposition to this expectation, with band positions decreasing as Fe content increases. We cannot confidently explain this conflict, but it is possible that the greater atomic weight of Fe relative to Mg may slow the vibrational frequency more than shortening T-O bonds can increase it.

5.3. Clinopyroxenes

5.3.1. Pigeonite. Monoclinic pyroxenes having ~5–15 mol % Ca are referred to as pigeonite. The emissivity spectrum of sample $Wo_{10}En_{36}Fs_{54}$ 33,34, a synthetic pigeonite, is shown in Figure 9. Despite the change in structure from orthorhombic (space group *Pbca*) to monoclinic ($P2_1/c$), the spectral character of pigeonite is similar to that of the orthopyroxenes (Figure 4) rather than the high-Ca clinopyroxenes (Figure 5). Between 1100 and 1000 cm^{-1}, the single feature (CA1) in orthopyroxene spectra is split into two bands in the pigeonite spectrum. The CA2 and CA3 (~950–970 cm^{-1}) features in orthopyroxenes may be comparable to the 950 cm^{-1} band in the pigeonite, and both spectra contain a prominent band (CA4 in opx) in the vicinity of 875 cm^{-1}. The broad spectral features between 850 and 650 cm^{-1} in the pigeonite spectrum are due to anomalous scattering in the sample, which is very fine grained, and would not appear in the spectrum of a coarse particulate sample. In the range from 600 to 400 cm^{-1} the pigeonite and orthopyroxene spectra are also similar, having a strong absorption feature near 500 cm^{-1}, with weaker absorptions on both the short- and long-wavelength sides of the band. In summary, it appears from this pigeonite sample that the primary spectral effect of adding calcium to the orthopyroxene structure (thus making a low-Ca clinopyroxene) is to alter the shapes of the shortest wavelength (T-O stretching) feature(s). Differences in the region of T-O bending (longer wavelengths) are more subtly expressed as variations in band position, without addition or removal of significant absorption features.

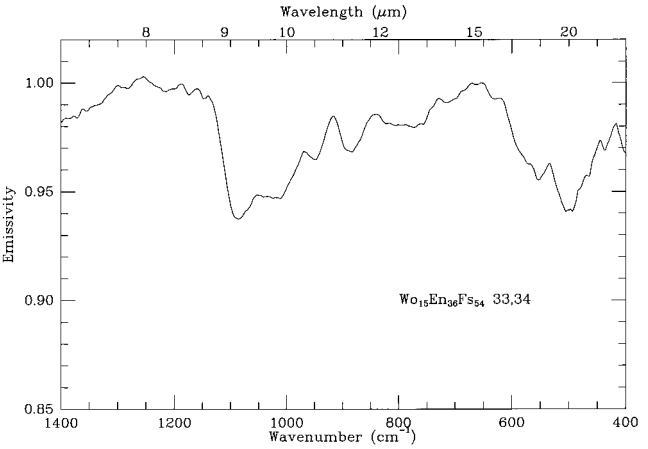

Figure 9. Emissivity spectrum of pigeonite $Wo_{10}En_{36}Fs_{54}$ 33,34.

5.3.2. High-calcium clinopyroxenes. High-Ca clinopyroxenes (henceforth referred to as clinopyroxenes, space group *C*2/*c*) have fewer absorption features than their orthorhombic counterparts (compare Figures 4 and 5). As in orthopyroxene spectra, the absorptions in clinopyroxene spectra also exhibit characteristic variations in location that are linked to the relative amounts of Mg and Fe in the sample as well as Ca, Na, and Mn. Table 4 lists the average position of the band minima for the critical absorptions of clinopyroxenes. Historically, clinopyroxene nomenclature has been variable, but the International Mineralogical Association [*Morimoto*, 1989] defines diopside and hedenbergite as the end-member compositions $CaMgSi_2O_6$ and $CaFe^{2+}Si_2O_6$, respectively, and augite as the solid solution mineral $(Ca,Mg,Fe^{2+})_2Si_2O_6$. Variations in composition are described by Mg/(Mg + Fe) or by the molecular percentage of each end-member (Wo, En, and Fs).

Other cations may substitute into the quadrilateral clinopyroxenes in nontrace amounts (e.g., Al^{3+} and Ti^{4+}), but no correlations between band position and abundances of these

Table 4. Positions of Critical Absorptions in Clinopyroxenes

Sample	Mg/(Mg+Fe)	Band Position, cm^{-1}				
		CA1	CA2	CA3	CA4	CA5
VEH-DIO01	0.98	1116	961	921	559	486
DSM-DIO01	0.98	1120	961	916	560	482
NMNH-107497	0.97	1114	960	918	548	479
WAR-6454	0.96	1111	960	918	551	476
HS-317.4B	0.93	1085	957	912	552	482
BUR-1820	0.92	1109	960	921	555	480
WAR-5780	0.92	1112	961	921	546	479
HS-15.4B	0.92	1120	959	921	560	471
NMNH-80819	0.90	1104	961	920	553	483
NMNH-R15161	0.87	1109	961	919	552	481
WAR-5858	0.81	1088	960	907	546	478
NMNH-119197	0.81	1107	960	917	549	481
NMNH-R17421	0.78	1105	960	919	551	479
DSM-AUG01	0.75	1085	961	918	538	480
NMNH-122302	0.74	1090	956	915	539	489
HS-119.4B	0.68	1117	947	914	549	478
WAR-6474	0.58	1101	944	919	541	477
NMNH-9780	0.51	1082	959	875	517	471
BUR-620	0.45	1098	943	917	530	476
NMNH-16168	0.45	1102	941	911	536	471
DSM-HED01	0.36	1114	937	970	532	469
HS-10.4B	0.26	1077	947	883	505	464
NMNH-R11524	0.07	1091	953	886	517	464
Average		1102	955	915	543	477
Standard deviation		13	8	18	15	6
Minimum λ		1077	937	875	505	464
Maximum λ		1120	961	970	560	489
Δλ		43	24	95	55	25

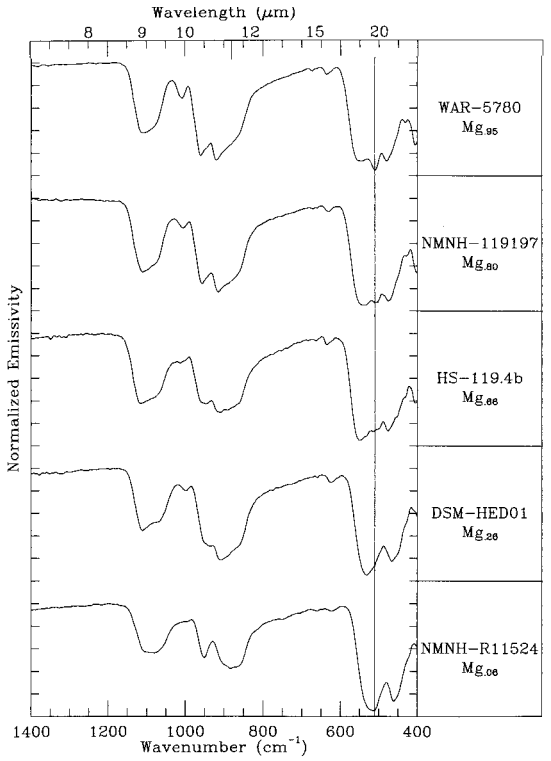

Figure 10. Emissivity spectra of clinopyroxenes with 50 mol % Ca along the Mg-Fe join. Subscripts refer to the fraction of M1 sites filled by Mg. The vertical line denotes the location of the 515 cm^{-1} feature.

cations are observed. Substitution of Al^{3+} for Si^{4+} in the tetrahedral site (Al/(Al + Si) = 0.0 to ~0.375), in particular, can produce significant, linearly correlated variations in the T-O distance [*Cameron and Papike*, 1981]. However, in this suite of clinopyroxenes the range of Al/(Al + Si) values is not very large (0.005–0.10) and is therefore unlikely to produce noticeable spectral effects (Figure 10).

5.3.3. Critical absorption variation with Mg-Fe substitution. As in the case of the orthopyroxenes, assignment of the CA1 band minimum may be difficult due to the broadness of the band; however, the position of the band minima for CA1–CA5 in the clinopyroxenes is generally shifted to longer wavelengths (lower wavenumbers) with increasing Fe content (Figures 11 and 12). This trend is most apparent in samples with less than Mg_{70-80}.

The structural effect of substituting Fe^{2+} for Mg^{2+} in clinopyroxene is to increase the mean ionic radius ($^{VI}M1$ + $^{VI}M2$). The increased size of the octahedral layer results in a decrease in the tetrahedral chain angle as well as an increase in the tetrahedral size and mean T-O (bridging) angle [*Cameron and Papike*, 1981]. Although it is difficult to ascertain exactly which of these T-O bond vibrations are dominating the mineral spectrum, it is possible that the increase in the tetrahedral size with increasing Fe^{2+} in M2, as well as the greater atomic weight of Fe^{2+}, produces the shift to lower wavenumbers of the CA1–CA5 band positions as T-O bonds lengthen.

5.3.4. Critical absorption variation with Ca abundance. Unlike orthopyroxenes, the spectral characteristics observed in samples from the clinopyroxene solid solution series are variable not only with relative Mg-Fe content, but also with differences in Ca abundance, and two distinct Ca-related trends are observed. First, with decreasing Ca content, the reststrahlen bands between 1200 and 800 cm^{-1} become less sharp and commonly exhibit less spectral contrast. Figure 12 shows a pair of spectra (NMNH-R17421 and WAR-6474) that have similar Mg/(Mg + Fe) ratios but have "high" and "low" Ca contents. (The second pair in Figure 12, NMNH-16168 and BUR-620, displays the same characteristics, but with a more Fe-rich Mg/(Mg + Fe) ratio than the first pair). Compositions having 45–50 mol % Ca typically have the sharpest features (NMNH-R17421 and NMNH-16168 in Figure 12), which make band minimum identification easier than in lower Ca samples, which tend to have broader features and may display minor features that are not observed in the higher calcium samples

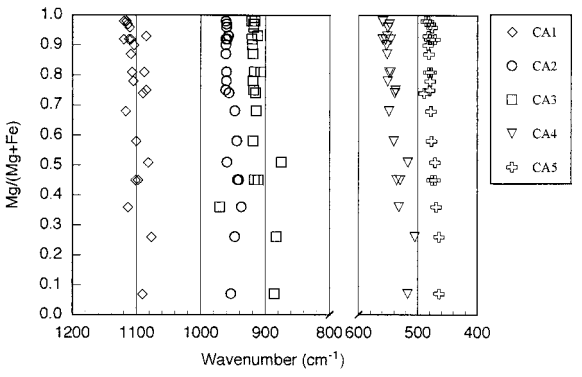

Figure 11. Scatterplot of quadrilateral clinopyroxene CA1–CA5 band position versus Mg/(Mg + Fe). Error bars along the wavenumber axis are smaller than the dimension of the symbols.

(WAR-6474 and BUR-620 in Figure 12). Second, in low-Ca samples containing Na (see above pairs in Figure 12), the CA2 band (~960 cm^{-1}) is reduced in strength and reveals an adjacent weak band minimum at ~945 cm^{-1}. This is not observed in NMNH-9780 (Figure 12), a sample that contains <45 mol % Ca but contains no Na.

A decrease in spectral contrast and feature sharpness in clinopyroxene spectra is probably related to the population of the M2 site through the effect of this population on the tetrahedral chain structure and T-O bonds. Cases in which the greatest amounts of Ca are contained in the M2 cation site produce the most regular structure because the majority of M2 sites are the same size. Because the majority of the octahedral sites are similar, the tetrahedral chain experiences fewer distortions around the octahedral sites, and the majority of the T-O bonds within the tetrahedral chain should vibrate similarly. Hence the clearest spectral representations of the primary clinopyroxene vibrations are probably exhibited by the clinopyroxenes with the highest abundances of Ca. In contrast, the M2 sites of clinopyroxenes with reduced Ca abundances are populated by a greater number of different cations (e.g., smaller Fe^{2+} atoms, or monovalent Na), and the size or electrostatic environment of the M2 octahedron around those atoms is changed. The altered octahedral size or bonding may induce local distortions in the tetrahedral chain, altering T-O bond lengths and resulting in additional vibrational modes. Additional vibrational modes may be exhibited as a reduction in spectral contrast and/or the appearance of additional features in the spectrum of the mineral.

The second trend observed with reduced Ca abundances is related to Na substitution. Figure 12, as described above, shows a comparison of two high calcium diopsides (samples NMNH-R17421 and NMNH-16168) to the spectra of two augites with similar Mg/(Mg + Fe), but having less than 45 mol % Ca (samples WAR-6474 and BUR-620). In both low-Ca cases, there is ~7–7.5 mol % Na present, which fills the remaining M2 sites. These Na-bearing augites are distinguished from high-Ca clinopyroxene by the presence of a weak feature at ~883 cm^{-1} and from an augite without Na, NMNH-9780, by a substantially different band shape in the same region. Although Na and Ca have very similar ionic radii, their electrostatic environments are different because Na^+ is monovalent, whereas Ca^{2+} is divalent. When Na^+ is substituted for Ca^{2+}, the charge deficiency of Na^+ must be accommodated, and commonly, Fe^{3+} makes a paired substitution with Na^+. Although microprobe analysis cannot distinguish between Fe^{2+} and Fe^{3+}, both Na-augites are estimated to have ~10 mol % Fe^{3+} on the basis of charge balance considerations. In both cases there is thus an excess of Fe^{3+} relative to the Na^+ that must be accommodated. In both cases the amount of excess Fe^{3+} is approximately equivalent to the amount of $^{IV}Al^{3+}$ in the T site, thus balancing the remaining Fe^{3+}. Therefore, although the M2 site size may not change significantly, the accompanying substitutions result in changes in both the electrostatic environment of the M2 site and the size of the M1 and T sites, all of which change T-O bond character and are the most likely sources of the changes in vibrational character of these samples.

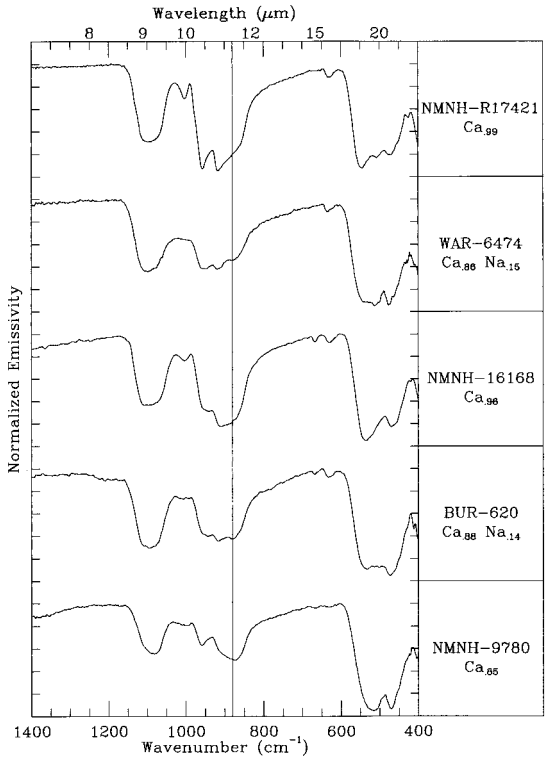

Figure 12. Emissivity spectra of Ca-rich and Ca-poor quadrilateral clinopyroxenes. The vertical line denotes the location of the 883 cm^{-1} feature, and subscripts refer to the fraction of M2 sites occupied.

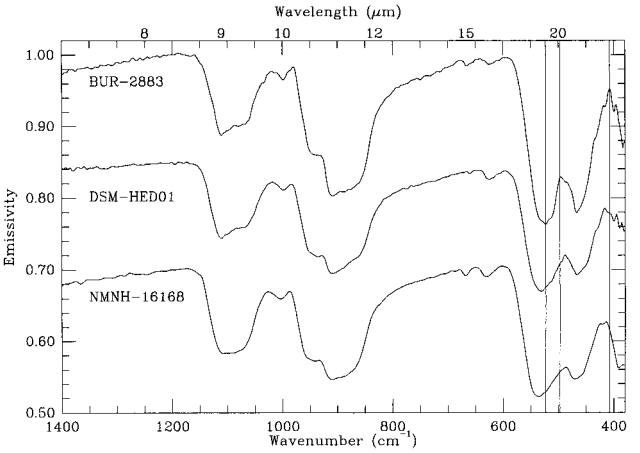

Figure 13. Emissivity spectra of johannsenite BUR-2883 ($Wo_{50}En_6Fs_9Jo_{36}$) and clinopyroxenes DSM-HED01 ($Wo_{49}En_{13}Fs_{24}Jo_{14}$) and NMNH-16168 ($Wo_{49}En_{22}Fs_{27}Jo_3$). Vertical lines denote the locations of spectral features described in the text. Spectra are offset by 0.15 for clarity.

5.3.5. Critical absorption variation with Mn abundance. Manganese is commonly found in Fe-rich clinopyroxenes in abundances of up to 4 wt % MnO [*Deer et al.*, 1992], and it is likely that there is some solid solution between the Ca-pyroxenes and the Mn-rich end-member johannsenite ($Ca(Mn,Fe)Si_2O_6$) [*Deer et al.*, 1992; *Cameron and Papike*, 1981]. Although not considered one of the quadrilateral pyroxene compositions, johannsenite will be discussed here in the context of variations in Mn content in the quadrilateral samples. Johannsenite BUR-2883, $Wo_{50}En_6Fs_9Jo_{36}$ (~21 wt % MnO), where Jo represents the Mn end-member, is slightly enriched in a quadrilateral component. Two samples will be compared to BUR-2883: DSM-HED01, $Wo_{49}En_{13}Fs_{24}Jo_{14}$ (8

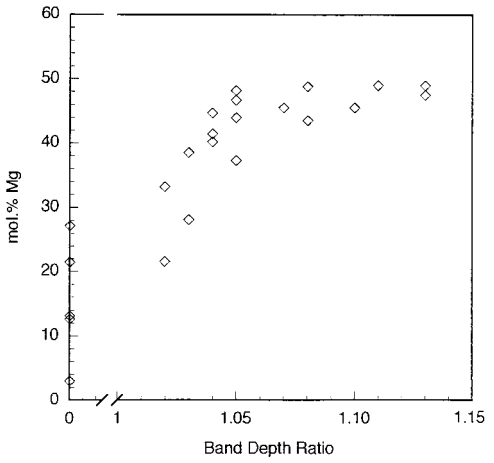

Figure 14. Scatterplot of clinopyroxene ~515 cm^{-1} band depth ratio versus mol % Mg.

wt % MnO), and NMNH-16168, $Wo_{49}En_{22}Fs_{27}Jo_3$ (<2 wt % MnO).

Fe-rich clinopyroxene and johannsenite spectra exhibit several similarities in band shape (Figure 13), a characteristic previously observed by *Rutstein and White* [1971] in transmission spectra. In the Rutstein and White study the most noticeable difference with the transition from Mg to Fe to Mn was the displacement of a sharp band near 900 cm^{-1} (CA3). In the present work we do not clearly observe this trend, although CA3 in johannsenite is much deeper relative to CA2 than in the quadrilateral samples (Figure 13), a trend which holds true when compared to the range of clinopyroxene solid solution compositions. Additional variations between the johannsenite spectrum and the Fe-rich clinopyroxene spectra are also observed. Between 600 and 400 cm^{-1}, johannsenite is similar to the Fe-rich quadrilateral pyroxenes in having only two absorptions, CA4 and CA5. The position of CA4 in BUR-2883 is ~520 cm^{-1}, but as Mn content decreases, the band is located at higher wavenumbers (shorter wavelengths), 532 cm^{-1} in DSM-HED01 and 536 cm^{-1} in NMNH-16168. The CA4 feature also becomes broader with decreasing Mn content, as demonstrated by the vertical line at ~500 cm^{-1} in Figure 13, which is placed to coincide with the long-wavelength emission maximum adjacent to CA4 in johannsenite. An emission maximum at ~405 cm^{-1} in johannsenite is also displaced to higher wavenumbers as Mn content decreases.

Because johannsenite has the same crystal structure as the clinopyroxenes (C_2/c) and appears to form a solid solution with the clinopyroxenes, it is not unusual that the spectra of johannsenite and quadrilateral clinopyroxenes look quite similar. Mn^{2+} may substitute into the clinopyroxene structure in either the M1 or M2 site; however, because all three samples described above have M2 sites that are almost completely filled with Ca and have insufficient Mg^{2+} and Fe^{2+} to fill the M1 site, the majority of the Mn^{2+} in these samples must be in the M1 site. The Mn^{2+} ion is larger than both the Fe^{2+} and Mg^{2+} ions, resulting in an increase in the size of the M1 site when Mn^{2+} is substituted. As the mean ionic radius of $^{VI}M1 + {}^{VI}M2$ increases, the mean T-O distance also increases. Assuming no other significant changes, an increase in the T-O distance results in longer bonds that should vibrate more slowly, which is consistent with the observation that CA4 and nearby spectral features are at lower wavenumbers (longer wavelengths) with increased Mn content. Although the Fe-rich clinopyroxenes DSM-HED01 and NMNH-16168 contain small amounts of Mn, they do not exhibit the differences (relative to CA2-CA3 band depth, CA4 band position and width, and location of the longest wavelength emission maximum) that the johannsenite sample displays relative to the quadrilateral clinopyroxenes. This determination suggests that these spectral characteristics are only distinguishable in samples with Mn contents greater than the typical amounts observed in quadrilateral pyroxenes.

5.3.6. Additional features. A spectral absorption between CA4 and CA5 (near 515 cm^{-1}) is not consistently present in all clinopyroxene spectra. The "disappearance" of this band is shown by a ratio of the emissivity of the 515 cm^{-1} band minimum to the emissivities of the maxima immediately adjacent to the band (Figure 14). This ratio is expressed as $(\varepsilon_{max1}/\varepsilon_{min})/(\varepsilon_{min}/\varepsilon_{max2})$, where ε_{max1} is the emissivity maximum on the short-wavelength side of 515 cm^{-1}, ε_{min} is the band minimum, and ε_{max2} is the emissivity maximum on the long-wavelength side of 515 cm^{-1}. With increasing Fe content, this band is apparently reduced in emissivity (Figures 5 and 10) and is not at all distinguishable in samples with compositions having <20 mol % Mg; of four samples with 20–30 mol % Mg, two samples display a weak 515 cm^{-1} feature and two do not. Thus the presence (and strength) or absence of the 515 cm^{-1} band may be used to broadly classify an unknown sample as either Mg- or Fe-rich. As the feature gradually disappears, there is no progressive variation in its position; therefore it is either becoming reduced in emissivity or is being masked as the adjacent CA4 band migrates to longer wavelengths (or some combination of both). Another small but distinctive absorption at ~1010 cm^{-1} usually present in the spectra of Ca-rich (>45 mol % Ca) samples is either substantially reduced in strength or is not present at all in the low-Ca compositions.

The reduction in depth of some bands is probably attributable to the same effect as in the case of band position shifts described above, i.e., increasing numbers of heterogeneous

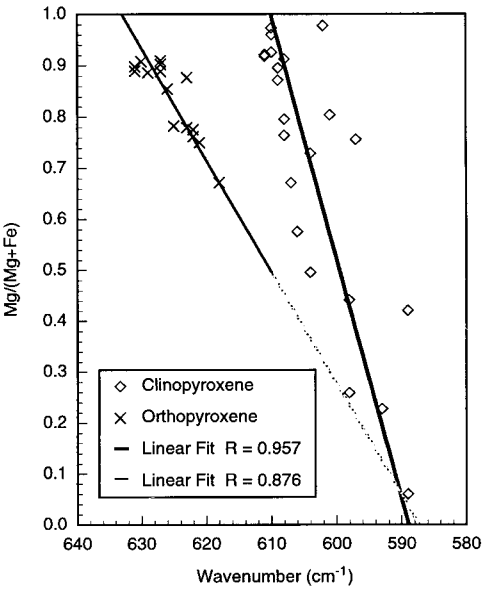

Figure 15. Scatterplot of secondary Christiansen feature position versus Mg/(Mg + Fe). Error bars along the wavenumber axis are smaller than the dimension of the symbols.

vibrational modes due to increased distortions of the tetrahedral chain around octahedral sites of variable coordination.

5.4. Secondary Christiansen Feature

At certain wavelengths in the emissivity spectra of silicate minerals, emissivity is (or is close to) unity, and these features are referred to as Christiansen maxima. The Christiansen maximum is directly associated with the Christiansen frequency, which is the frequency at which the real part of the refractive index of the sample, n, equals 1 [*Henry*, 1948; *Conel*, 1969; *Hapke*, 1993]. This region of anomalous dispersion is located at a slightly shorter wavelength than the fundamental vibrational mode with which it is associated, and absorption is low, resulting in an emission maximum. Because the emission maximum does not exactly coincide with the Christiansen frequency, it is referred to as a Christiansen maximum, or Christiansen feature [*Salisbury*, 1993]. These emission maxima may also be displaced due to environmental factors such as atmospheric pressure [*Logan et al*., 1973; *Salisbury*, 1993; see also *Hapke*, 1993], although this effect is minimal within the variability of terrestrial pressures. The "primary" Christiansen feature is associated with the strongest vibrational features; for silicates this is in the region of 1350–1100 cm^{-1} (~7.5–9 μm) on the short-wavelength side of the Si-O stretching feature [*Salisbury*, 1993; *Hapke*, 1993]. In this study a similar feature on the short-wavelength side of the Si-O bending region (600–400 cm^{-1}) will be referred to as the secondary Christiansen feature.

The general position of the secondary Christiansen feature is diagnostic in quadrilateral pyroxenes. Plotting the wavenumber position of the secondary Christiansen feature on a correlation chart versus Mg/(Mg + Fe) allows discrimination of orthorhombic and monoclinic pyroxenes (Figure 15). Furthermore, the relative Mg/(Mg + Fe) ratio of minerals within each structural group may be estimated from the location of this feature, as there is a roughly linear trend between composition and the location of this Christiansen feature.

6. Nonquadrilateral Pyroxenes

Nonquadrilateral pyroxenes contain significant amounts of Na^+, Fe^{3+}, Al^{3+}, and Li^+ in the M1 and M2 sites [*Papike et al*., 1974]. End-member compositions include acmite ($NaFe^{3+}Si_2O_6$), jadeite ($NaAlSi_2O_6$), and spodumene ($LiAlSi_2O_6$). Acmite (also referred to as aegirine) is typically found in alkaline and peralkaline rocks such as alkali granites and syenites. Some solid solution with augite (aegirine-augite) is possible in regionally metamorphosed rocks such as glaucophane- and riebeckite-bearing schists [*Deer et al*., 1992]. Jadeite is dominantly found in metamorphic rocks, and spodumene is a characteristic mineral of Li-rich granitic pegmatites [*Deer et al*., 1992]. Jadeite and spodumene compositions rarely deviate from their ideal formulas, although some excess Si (>2 atoms per formula unit based on 6 oxygens) may be found in spodumene. All of the nonquadrilateral compositions belong to space group $C2/c$, like the quadrilateral Ca-pyroxenes. (The only naturally occurring spodumene is α-spodumene ($C2/c$), but other high-temperature polymorphs (β- and γ-spodumene) having tetragonal and hexagonal space groups are possible [*Deer et al*., 1978].)

There are a total of five high-quality nonquadrilateral samples in the suite studied: three spodumenes, one acmite, and one jadeite. Because of the small number of samples, conclusions regarding the links between their crystal chemistry and their spectra are subject to revision as more samples are acquired in the future.

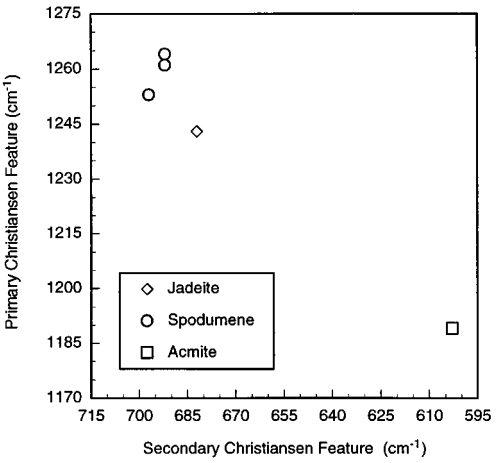

Figure 16. Scatterplot of primary Christiansen feature position versus secondary Christiansen feature position for nonquadrilateral pyroxenes. Error bars along the wavenumber axis are smaller than the dimension of the symbols.

The TIR spectra of nonquadrilateral compositions exhibit a significantly different morphology than the spectra of the quadrilateral minerals (Figure 3), permitting their rapid identification as nonquadrilateral compositions. Spectra of these minerals are very similar in shape, having a single, broad feature with smaller superposed features in the 1200–800 cm^{-1} region rather than the multiple bands observed in the spectra of quadrilateral orthopyroxenes and clinopyroxenes. The overall shape of the feature broadens within the series, ranging from ~1150 to 850 cm^{-1} in acmite to 1200–850 cm^{-1} in jadeite and 1250–850 cm^{-1} in spodumene. The increasing wavenumber position of the T-O stretching absorption features is correlated with the decreasing ionic radii of the cations. Acmite, with the largest mean ionic radius, should vibrate more slowly (lower frequencies, longer wavelengths) than jadeite, which has a smaller mean ionic radius. Smaller still is the Li-Al cation pair in spodumene, which exhibits the highest wavenumber (highest frequency, shortest wavelength) absorption features of the three minerals. The reststrahlen features at long wavelengths, between 700 and 400 cm^{-1}, also become progressively broader in the transition from acmite to jadeite to spodumene.

The differences between the spectra of sodic and lithium pyroxenes and quadrilateral compositions can be related to the occupancy of the M cation sites, their distortions, and the subsequent influence on the tetrahedral chain angle and T-O bond lengths. As in the Ca-pyroxenes, the tetrahedral chain angle in Na-pyroxenes decreases with increasing mean ionic radius in the M sites ($^{VI}M1 + {}^{VI}M2$). However, the chain angles in Na-pyroxenes are 5–10° larger for a given mean ionic radius than the Ca-pyroxenes (i.e., the mean chain angle is greater when M2 is smaller) because the mean ionic radius of the Na-pyroxenes is smaller than that of the Ca-pyroxenes [*Cameron and Papike*, 1981]. Because Ca^{2+} and Na^+ are not significantly different in size, the greatest contribution to the difference in mean ionic radius between the Ca- and Na-pyroxene series comes from the replacement of Mg^{2+} in the quadrilateral minerals by Fe^{3+} and Al^{3+} in the sodic compo-

sitions. As the size of the M1 cation increases within the Na-pyroxene series (from Al-bearing jadeite to Fe^{3+}-bearing acmite), the tetrahedral chain becomes more kinked because the M1 octahedron increases in size, and the octahedral edge is also enlarged [*Cameron and Papike*, 1981]. The straightening of the chain is accommodated by an increase in the T-O (bridging) distances. In pure spodumene the mean chain angle is greater than that of the Na-pyroxenes (consistent with the significantly smaller M2 lithium cation) and is actually 190°, which physically correlates to an opposing rotational sense. Unlike the Na-pyroxenes, the linkage between the octahedral and tetrahedral layers is accommodated by expanding the tetrahedral edge (rather than the octahedral edge) and increasing the angle of O-T-O [*Hawthorne and Grundy*, 1977].

Spectra of nonquadrilateral minerals exhibit variability in their secondary Christiansen feature positions similar to that exhibited by the Mg-Fe pyroxenes and the Ca-pyroxenes. In addition, variations in the position of the primary Christiansen feature are also prominent in the nonquadrilateral series as described above. A plot of the primary versus secondary Christiansen feature position can be used to distinguish between the three end-members (Figure 16).

A greater understanding of the relationships between the crystal chemistries and spectral characteristics of nonquadrilateral pyroxenes could be obtained with the acquisition of not only more end-member samples, but samples in the solid solution region between Ca-pyroxene and Na-pyroxene (i.e., omphacites and aegirine-augites). Data from these minerals should permit a better tracking of the spectral transitions between quadrilateral and sodic compositions.

7. Application to Unknown Sample Identification

7.1. Laboratory Samples

Many compositional analysis instruments, such as the electron microprobe, require long-duration, multiple-point analyses and/or extensive sample preparation. TIR emission and reflectance measurements, on the other hand, do not require long sample analysis times, nor do they require that the sample be specially prepared. Bulk samples and crushed samples may be analyzed, and no sample mounting is necessary. Thus for basic compositional analysis of an unknown sample, the infrared technique may be an easy, time saving tool.

Based on the pyroxene samples examined thus far, several constraints may be placed on the ability to identify unknown samples via their thermal infrared spectra, using the number of absorption features, band shapes, and band positions in a process that progressively narrows down to the appropriate composition. Structural determination (clino- versus ortho-) is relatively straightforward on the basis of spectral morphology (i.e., the number of emissivity minima and their relative locations). If the sample is a quadrilateral pyroxene, the relative Mg-Fe content may be approximately established by plotting the wavenumber positions of several diagnostic spectral features on the plots presented in this paper. For high-Ca clinopyroxenes, Ca-rich and Ca-poor varieties also can be distinguished, as well as Na substitution. Some spectra of unknown samples may exhibit characteristics like those described here for the nonquadrilateral pyroxenes, such as a single broad feature at short wavelengths. If so, the simplest way to distinguish whether the sample is acmite, jadeite, or spodumene is to plot the positions of the primary and secondary Christiansen features. If a sufficiently broad spectral library is available, band matching or linear deconvolution algorithms may be used to identify samples even more rapidly than could be done by hand.

7.2. Identification in Complex Lithologies and Remote Sensing Data

Throughout this paper, the discussion of pyroxene discrimination and identification from TIR spectra has focused on pure physical samples in a laboratory setting, but the ability to identify and discriminate between pyroxenes (and other minerals) in rock samples or in planetary remote sensing data sets has important implications for broader applications of the data presented here. Clearly, the level of detail with which we have examined pyroxene spectral systematics is unlikely to be resolvable in the real world of remote sensing. TIR spectra acquired by remote sensing instruments are not sampling pure minerals, but rather a complex mixture of atmospheric constituents and multimineralic rocks, if not mixtures of rocks and other surface materials (e.g., soils and vegetation). Remotely acquired spectra also commonly have lower signal-to-noise and/or lower spectral resolution than laboratory data. However, this does not preclude identification of pyroxenes in spectra of mixed surfaces, or even additional details of structure and composition.

At sufficiently large particle sizes (greater than ~65 μm) and in solid samples the spectrum of a physical mixture is the same as the spectrum derived by adding the component mineral spectra linearly in proportion to their abundance [*Christensen et al*., 1986; *Crown and Pieters*, 1987; *Thomson and Salisbury*, 1993]. In the reverse sense, mixture spectra can be deconvolved in order to determine the component minerals and their abundances [*Johnson et al*., 1983, 1992; *Sabol et al*., 1992; *Mustard and Pieters*, 1989; *Ramsey and Christensen*, 1998]. *Hamilton and Christensen* [this issue] applied the linear least squares deconvolution algorithm of *Ramsey and Christensen* [1998] to a collection of spectra of pyroxene-bearing mafic and ultramafic rocks. The linear deconvolution technique was successful not only in determining the rocks' modal mineralogy, but also in distinguishing between orthopyroxene and clinopyroxene, the approximate pyroxene Mg-Fe solid solution composition, and the general composition of other components such as plagioclase feldspar [*Hamilton and Christensen*, this issue]. Because linear deconvolution has been demonstrated to make these distinctions, the diagnostic features of pyroxenes described in this paper, although not individually distinguishable in a multimineralic spectrum, clearly must contribute to the spectrum.

Remote sensing instruments typically must sacrifice either spatial or spectral resolution in order to meet power and/or data rate constraints. For example, the Mariner 6 and 7 infrared spectrometer (IRS) instruments obtained TIR spectral data of Mars with 2 cm^{-1} sampling; however, the spatial resolution was of the order of hundreds of kilometers. The Mars Global Surveyor Thermal Emission Spectrometer (TES) has a lower spectral resolution (selectable 5 or 10 cm^{-1} sampling) but achieves a greater spatial resolution (3 km per pixel). At lower spectral sampling there is the potential for spectral features to become less well resolved. Figure 17 shows the spectra of an orthopyroxene and a clinopyroxene at 2, 5, and 10 cm^{-1} spectral sampling, the latter two coinciding with the exact bandpasses of the TES. Spectra with 5 cm^{-1} sampling are virtually indistinguishable from the 2 cm^{-1} data, except for a

slight decrease in the apparent smoothness of the narrowest band minima. At 10 cm^{-1} sampling this effect is greater, but all of the original band minima are still apparent. Clearly, for narrow diagnostic features that vary in band position by only a few wavenumbers, variations between samples will no longer be resolvable at 10 cm^{-1} sampling (e.g., opx CA2, Figure 18b and Table 3). However, bands that vary in position by greater amounts (e.g., opx CA1) will remain sufficiently resolved to permit them to be used for identification purposes (Table 3 and Figure 18a, compare to Figure 7a). In fact, when laboratory spectra of rocks are convolved to 10 cm^{-1} sampling and run through the linear deconvolution algorithm, the decrease in accuracy of modal abundance determination is only about 10% [*Hamilton*, 1999; *Hamilton and Christensen*, this issue]. Finally, deconvolution analyses of TES spectra of Mars are successfully distinguishing mineral components with compositions and abundances that are consistent with laboratory studies of similar spectral shapes and are geologically plausible. These results suggest that the careful application of the detailed laboratory analyses described in this paper to the interpretation of remote sensing data is legitimate [*Christensen et al.*, this issue, (a)].

8. Conclusion

The thermal emission spectra of pyroxenes exhibit a large number of variations in band shape, depth, and position that are related to systematic changes in crystal structure and chemistry. The trends in these variations can be used to determine the structure and general composition of an unknown sample, including the ability to determine relative quadrilateral or nonquadrilateral composition, quadrilateral solid solution, and major element cation substitutions. Combined application of these determinative characteristics to the discrimination of pyroxene compositions in the laboratory may allow for faster initial analysis of unknown samples. This increased understanding of the spectral variability of pyroxenes will also allow for greater confidence in a higher level of geologic interpretation than might otherwise be possible in remote sensing data.

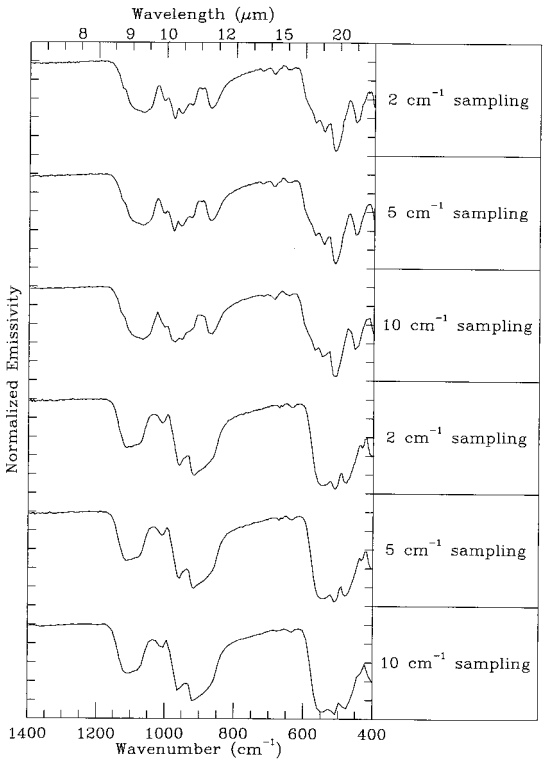

Figure 17. Plot of orthopyroxene and clinopyroxene at 2, 5, and 10 cm^{-1} sampling.

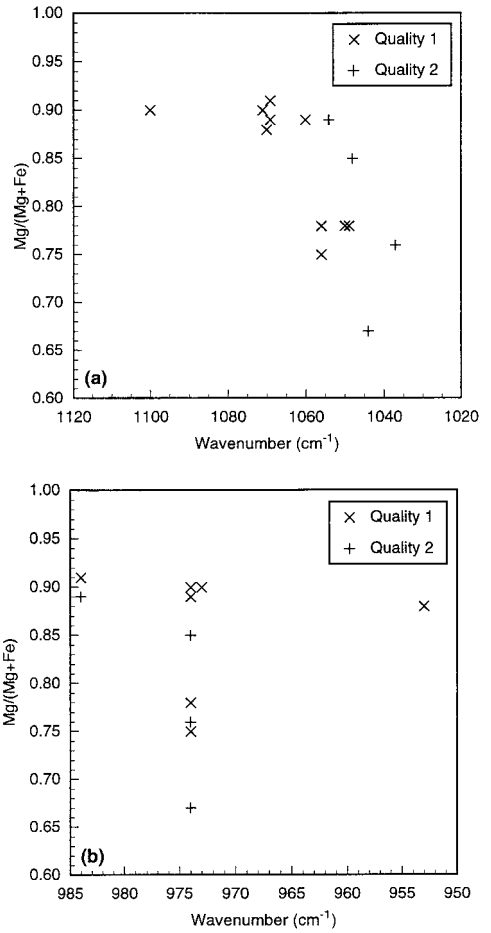

Figure 18. Scatterplot of orthopyroxene (a) CA1 band position at 10 cm^{-1} spectral sampling and (b) CA2 band position at 10 cm^{-1} spectral sampling.

Acknowledgments. I would like to extend my deep appreciation to the National Museum of Natural History (NMNH) at the Smithsonian Institution for donating the majority of samples used in this study. Additional samples were graciously provided by the USGS and Los Angeles County Museum of Natural History. I am especially grateful to Don Lindsley for synthesizing pigeonite $Wo_{15}En_{36}Fs_{54}$33,34 and to J. Holloway for assistance in synthesizing diopside sample VEH-DIO01. V.E.H. was supported by a National Physical Science Consortium Graduate Fellowship, with stipend support from the Jet Propulsion Laboratory. The author would like to thank J. Salisbury, M. Gaffey, and an anonymous reviewer for comments and suggestions that have helped improve the manuscript.

References

Adams, J. B., Visible and near infrared diffuse reflectance spectra of pyroxenes as applied to remote sensing of solid objects in the solar system, *J. Geophys. Res.*, *79*, 4829–4836, 1974.

Bancroft, G. M., and R. G. Burns, Interpretation of the electronic spectra of pyroxenes, *Am. Mineral.*, *52*, 1278–1287, 1967.

Cameron, M., and J. J. Papike, Structural and chemical variations in pyroxenes, *Am. Mineral*., *66*, 1–50, 1981.

Christensen, P. R., and S. T. Harrison, Thermal infrared emission spectroscopy of natural surfaces: Application to desert varnish coatings on rocks, *J. Geophys. Res*., *98*, 19,819–19,834, 1993.

Christensen, P. R., H. H. Kieffer, S. C. Chase, and D. D. Laporte, A thermal emission spectrometer for identification of surface composition from Earth orbit, in *Commercial Applications and Scientific Research Requirements for Thermal Infrared Observations of Terrestrial Surfaces*, *NASA-EOSAT Joint Report*, pp. 119–132, Earth Observ. Satell. Co., Lanham, Md., 1986.

Christensen, P. R., et al., Thermal Emission Spectrometer Experiment: The Mars Observer Mission, *J. Geophys. Res*., *97*, 7719–7734, 1992.

Christensen, P. R., J. L. Bandfield, M. D. Smith, and V. E. Hamilton, Identification of a basaltic component on the Martian surface from Thermal Emission Spectrometer data, *J. Geophys. Res*., this issue (a).

Christensen, P. R., J. L. Bandfield, V. E. Hamilton, D. A. Howard, M. D. Lane, J. L. Piatek, S. W. Ruff, and W. L. Stefanov, A thermal emission spectral library of rock-forming minerals, *J. Geophys. Res*., this issue (b).

Cloutis, E. A., and M. J. Gaffey, Pyroxene spectroscopy revisited: Spectral-compositional correlations and relationship to geothermometry, *J. Geophys. Res*., *96*, 22,809–22,826, 1991.

Conel, J. E., Infrared emissivities of silicates: Experimental results and a cloudy atmosphere model of spectral emission from condensed particulate mediums, *J. Geophys. Res*., *74*, 1616–1634, 1969.

Crown, D. A., and C. M. Pieters, Spectral properties of plagioclase and pyroxene mixtures and the interpretation of lunar soil spectra, *Icarus*, *72*, 492–506, 1987.

Deer, W. A., R. A. Howie, and J. Zussman, *Rock-Forming Minerals*, vol. 2A, *Single-Chain Silicates*, 2nd ed., 668 pp., John Wiley, New York, 1978.

Deer, W. A., R. A. Howie, and J. Zussman, *An Introduction to the Rock-Forming Minerals*, 2nd ed., 696 pp., Addison-Wesley-Longman, Reading, Mass., 1992.

Droop, G. T. R., A general equation for estimating Fe^{3+} concentrations in ferromagnesian silicates and oxides from microprobe analyses, using stoichiometric criteria, *Min. Mag*., *51*, 431–435, 1987.

Estep, P. A., Infrared spectra of lunar, meteoritic and terrestrial pyroxenes, *Geol. Soc. Am. Abstr. Programs*, *4*, 500, 1972.

Estep, P. A., J. J. Kovach, and C. Karr Jr., Infrared vibrational spectroscopic studies of minerals from Apollo 11 and Apollo 12 lunar samples, *Proc. Lunar Sci. Conf*., *2nd*, *3*, 2137–2151, 1971.

Estep, P. A., J. J. Kovach, P. Waldstein, and C. Karr Jr., Infrared and Raman spectroscopic studies of structural variations in minerals from Apollo 11, 12, 14, and 15 samples, *Geochim. Cosmochim. Acta Suppl. 3*, *3*, 3047–3067, 1972.

Evans, B. J., S. Ghose, and S. Hafner, Hyperfine splitting of ^{57}Fe and Mg-Fe order-disorder in orthopyroxene ($MgSiO_3$-$FeSiO_3$ solid solutions), *J. Geol*., *75*, 306–322, 1967.

Gaskell, P. H., The vibrational spectra of silicates, I, *Phys. Chem. Glasses*, *8*, 69–80, 1967.

Goldman, D. S., and G. R. Rossman, Determination of quantitative cation distribution in orthopyroxenes from electronic absorption spectra, *Phys. Chem. Min*., *4*, 43–53, 1979.

Hamilton, V. E., Linear deconvolution of mafic igneous rock spectra and implications for interpretation of TES data, *Lunar and Planet. Sci*. [CD-ROM], *XXX*, abstract 1825, 1999.

Hamilton, V. E., and P. R. Christensen, Determining the modal mineralogy of mafic and ultramafic igneous rocks using thermal emission spectroscopy, *J. Geophys. Res*., this issue.

Hapke, B., *Theory of Reflectance and Emittance Spectroscopy*, 455 pp., Cambridge Univ. Press, New York, 1993.

Hawthorne, F. C., and H. D. Grundy, Refinement of the crystal structure of $LiScSi_2O_6$ and structural variations in alkali pyroxenes, *Can. Min*., *15*, 50–58, 1977.

Henry, R. L., The transmission of powder films in the infrared, *J. Opt. Soc. Am*., *38*, 775–789, 1948.

Johnson, P. E., M. O. Smith, S. Taylor-George, and J. B. Adams, A semiempirical method for analysis of the reflectance spectra of binary mineral mixtures, *J. Geophys. Res*., *88*, 3557–3561, 1983.

Johnson, P. E., M. O. Smith, and J. B. Adams, Simple algorithms for remote determination of mineral abundances and particle sizes from reflectance spectra, *J. Geophys. Res*., *97*, 2649–2657, 1992.

Klein, C., and C. S. Hurlbut Jr., *Manual of Mineralogy*, 21st ed., 681 pp., John Wiley, New York, 1993.

Launer, P. J., Regularities in the infrared absorption spectra of silicate minerals, *Am. Mineral*., *37*, 764–784, 1952.

Lazarev, A. N., *Vibrational Spectra and Structure of Silicates*, 302 pp., Consult. Bur., New York, 1972.

Lazarev, A. N., and T. F. Tenisheva, The vibrational spectra of silicates, II, Infrared absorption spectra of silicates and germanates with chain anions, *Opt. Spectrom*., *10*, 37–40, 1961a.

Lazarev, A. N., and T. F. Tenisheva, The vibrational spectra of silicates, III, Infrared spectra of the pyroxenoids and other chain metasilicates, *Opt. Spectrom*., *11*, 316–317, 1961b.

Logan, L. M., G. R. Hunt, J. W. Salisbury, and S. R. Balsamo, Compositional implications of Christiansen frequency maximums for infrared remote sensing applications, *J. Geophys. Res*., *78*, 4983–5003, 1973.

Morimoto, N., Nomenclature of pyroxenes, *Can. Mineral*., *27*, 143–156, 1989.

Mustard, J. F., and C. M. Pieters, Photometric phase functions of common geologic minerals and applications to quantitative analysis of mineral mixture reflectance spectra, *J. Geophys. Res*., *94*, 13,619–13,634, 1989.

Omori, K., Analysis of the infrared absorption spectrum of diopside, *Am. Mineral*., *56*, 1607–1616, 1971.

Palluconi, F. D., and G. R. Meeks, Thermal infrared multispectral scanner (TIMS): An investigator's guide to TIMS data, 14 pp., *JPL Publ*., *85–32*, 1985.

Papike, J. J., K. L. Cameron, and K. Baldwin, Amphiboles and pyroxenes: Characterization of *Other* than quadrilateral components and estimates of ferric iron from microprobe data, *Geol. Soc. Am. Abstr. Programs*, *6*, 1053–1054, 1974.

Ramsey, M. S., and P. R. Christensen, Mineral abundance determination: Quantitative deconvolution of thermal emission spectra, *J. Geophys. Res*., *103*, 577–596, 1998.

Rossman, G. R., Lavender jade: The optical spectrum of Fe^{3+} and Fe^{2+}-Fe^{3+} intervalence charge transfer in jadeite from Burma, *Am. Mineral*., *59*, 868–870, 1974.

Ruff, S. W., P. R. Christensen, P. W. Barbera, and D. L. Anderson, Quantitative thermal emission spectroscopy of minerals: A laboratory technique for measurement and calibration, *J. Geophys. Res*., *102*, 14,899–14,913, 1997.

Rutstein, M. S., and W. B. White, Vibrational spectra of high-calcium pyroxenes and pyroxenoids, *Am. Mineral*., *56*, 877–887, 1971.

Ryall, W. R., and I. M. Threadgold, Evidence for $[(SiO_3)_5]_\infty$ type chains in inesite as shown by X-ray and infrared absorption studies, *Am. Mineral*., *51*, 754–761, 1966.

Sabol, D. E., J. B. Adams, and M. O. Smith, Quantitative subpixel spectral detection of targets in multispectral images, *J. Geophys. Res*., *97*, 2659–2672, 1992.

Saksena, B. D., Infra-red absorption studies of some silicate structures, *Trans. Faraday Soc*., *57*, 242–258, 1961.

Salisbury, J. W., Mid-infrared spectroscopy: Laboratory data, in *Remote Geochemical Analysis: Elemental and Mineralogical Composition*, edited by C. M. Pieters and P. A. J. Englert, 594 pp., Cambridge Univ. Press, New York, 1993.

Sunshine, J. M., C. M. Pieters, and S. F. Pratt, Deconvolution of mineral absorption bands: An improved approach, *J. Geophys. Res*., *95*, 6955–6966, 1990.

Thomson, J. L., and J. W. Salisbury, The mid-infrared reflectance of mineral mixtures (7–14 μm), *Remote Sens. Environ*., *45*, 1–13, 1993.

Virgo, D., and S. Hafner, Fe^{2+}-Mg order-disorder in natural orthopyroxenes, *Am. Mineral*., *55*, 201–223, 1970.

V. E. Hamilton, Department of Geology, Box 871404, Arizona State University, Tempe, AZ 85287-1404. (hamilton@tes.la.asu.edu)

(Received June 10, 1999; revised September 7, 1999;
accepted September 9, 1999.)